JEM Journal of Experimental Medicine

ARTICLE

Secreted mammalian DNases protect against systemic bacterial infection by digesting biofilms

Keenan A. Lacey[1*], Lee Serpas[2*], Sohei Makita[2*], Yueyang Wang[2], Ali Rashidfarrokhi[2], Chetna Soni[2], Sandra Gonzalez[1], Andre Moreira[2], Victor J. Torres[1,3], and Boris Reizis[2]

Extracellular DNase DNASE1L3 maintains tolerance to self-DNA in humans and mice, whereas the role of its homolog DNASE1 remains controversial, and the overall function of secreted DNases in immunity is unclear. We report that deletion of murine DNASE1 neither caused autoreactivity in isolation nor exacerbated lupus-like disease in DNASE1L3-deficient mice. However, combined deficiency of DNASE1 and DNASE1L3 rendered mice susceptible to bloodstream infection with *Staphylococcus aureus*. DNASE1/DNASE1L3 double-deficient mice mounted a normal innate response to *S. aureus* and did not accumulate neutrophil extracellular traps (NETs). However, their kidneys manifested severe pathology, increased bacterial burden, and biofilm-like bacterial lesions that contained bacterial DNA and excluded neutrophils. Furthermore, systemic administration of recombinant DNASE1 protein during *S. aureus* infection rescued the mortality of DNase-deficient mice and ameliorated the disease in wild-type mice. Thus, DNASE1 and DNASE1L3 jointly facilitate the control of bacterial infection by digesting extracellular microbial DNA in biofilms, suggesting the original evolutionary function of secreted DNases as antimicrobial agents.

Introduction

The majority of DNA in the mammalian organism is sealed in the nuclei and mitochondria of living cells and is rapidly cleared during cell death. The accumulation of host- or pathogen-derived DNA in inappropriate cellular compartments or extracellularly is a major danger signal that triggers immune activation through multiple sensing pathways (Barrat et al., 2016). Accordingly, the levels and location of DNA are controlled by several specialized mammalian DNases that prevent aberrant immune activation by self-DNA. Thus, DNA in the endolysosomes and cytosol is digested by DNase II and DNase III (TREX1), respectively, and their absence causes Aicardi-Goutières syndrome, a severe autoinflammatory disease (interferonopathy) driven by DNA-induced type I IFN production (Crow and Manel, 2015; Crowl et al., 2017). At the same time, DNases may facilitate processing of foreign DNA to ensure optimal immune responses. Thus, TREX1 digests DNA of reactivated endogenous retroelements as well as exogenous retroviruses such as HIV-1 (Volkman and Stetson, 2014). Furthermore, DNase II is required for antibacterial immunity in *Drosophila* (Seong et al., 2006) and for the processing of microbial DNA for recognition by its endosomal receptor TLR9 in mice (Chan et al., 2015).

The mammalian DNase I family of secreted DNases comprises DNASE1 and its three homologs (DNASE1L1–DNASE1L3), which are thought to digest extracellular DNA (eDNA; Keyel, 2017). Among the four family members, DNASE1L3 plays an essential role in maintaining immune tolerance to self-DNA. Null mutations in *DNASE1L3* in human patients cause monogenic systemic lupus erythematosus (SLE) characterized by early onset and antibody response to self-DNA (Al-Mayouf et al., 2011; Belot et al., 2020; Ozçakar et al., 2013). Moreover, many patients with severe sporadic SLE were recently found to develop blocking anti-DNASE1L3 antibodies that reduce the enzyme's activity in circulation (Hartl et al., 2021). Similar to humans, *Dnase1l3*-deficient mice on pure genetic backgrounds (both C57BL/6 and 129) develop anti–double-stranded DNA (dsDNA) and anti-nucleosome antibodies, progressive immune activation, and immune complex deposition in the kidneys (Sisirak et al., 2016; Weisenburger et al., 2018). This unique role of DNASE1L3 reflects its ability to digest DNA within the chromatin of apoptotic cells (Napirei et al., 2005; Sisirak et al., 2016; McCord et al., 2022), which enables the clearance of polynucleosomal DNA fragments associated with apoptotic

[1]Department of Microbiology, New York University Grossman School of Medicine, New York, NY, USA; [2]Department of Pathology, New York University Grossman School of Medicine, New York, NY, USA; [3]Antimicrobial-Resistant Pathogens Program, New York University Grossman School of Medicine, New York, NY, USA.

*K.A. Lacey, L. Serpas, and S. Makita contributed equally to this paper. Correspondence to Boris Reizis: boris.reizis@nyulangone.org; Victor J. Torres: victor.torres@nyulangone.org.

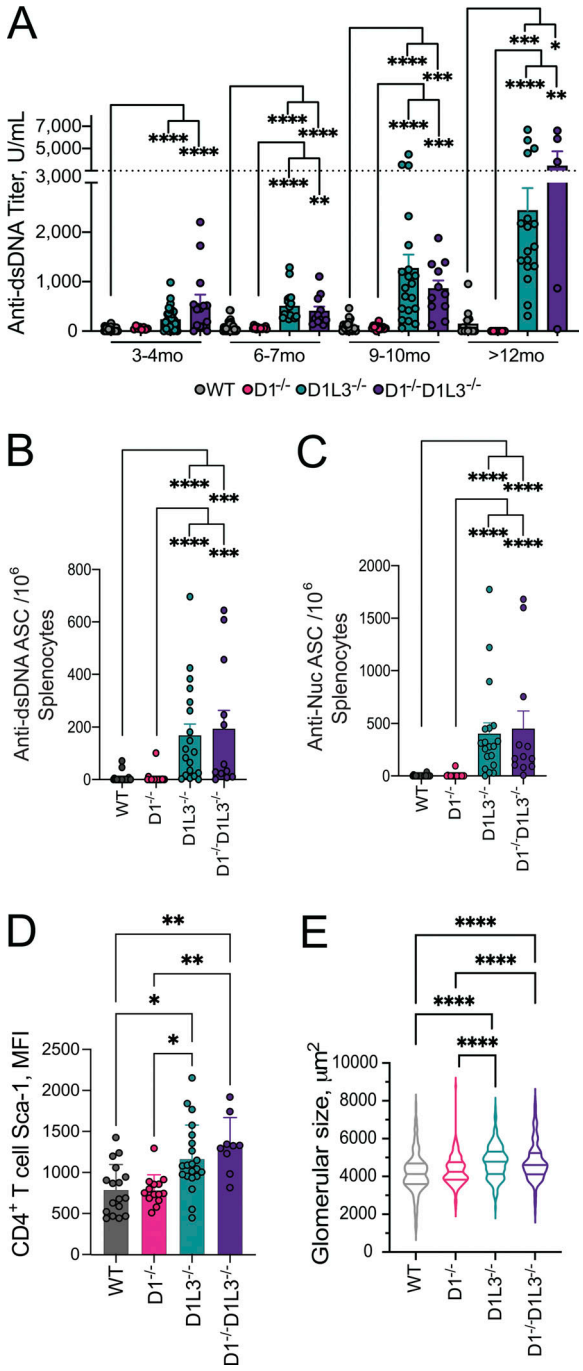

Figure 1. **DNASE1 deficiency does not cause or exacerbate autoreactivity to DNA. (A)** Serum titers of auto-Abs to dsDNA as determined by ELISA. Symbols represent individual mice; bars represent mean ± SEM. Groups of WT, $D1^{-/-}$, $D1L3^{-/-}$, and $D1^{-/-}D1L3^{-/-}$ mice were assessed at 3–4 mo (n = 33; 8; 36; 14), 6–7 mo (n = 33; 17; 19; 11), 9–10 mo (n = 17; 14; 20; 11), and >12 mo (n = 13; 7; 17; 5). **(B and C)** WT (n = 23), $D1^{-/-}$ (n = 19), $D1L3^{-/-}$ (n = 19), and $D1^{-/-}D1L3^{-/-}$ (n = 12) mice were assessed at 1 yr of age by ELISpot for the frequency of splenic antibody-secreting cells (ASC) reactive to dsDNA (B) and nucleosomes (C). Symbols represent individual mice; bars represent mean ± SEM. **(D)** $CD4^+$ T cells from the spleens of 1-yr-old WT (n = 17), $D1^{-/-}$ (n = 14), $D1L3^{-/-}$ (n = 21), and $D1^{-/-}D1L3^{-/-}$ (n = 9) mice were assessed for the expression of Sca-1 by flow cytometry. Symbols represent individual mice; bars represent mean ± SEM. **(E)** The sizes of glomeruli in the kidneys of mice of indicated genotypes at 1 yr of age. Shown are violin plots with median (thick lines) and quartiles (thin lines). At least 50 glomeruli from a single kidney section from WT (n = 6), $D1^{-/-}$ (n = 6), $D1L3^{-/-}$ (n = 6), and $D1^{-/-}D1L3^{-/-}$ (n = 6) mice were measured. Statistical significance was determined by Kruskal–Wallis test followed by Dunn's multiple-comparison test except for E, where one-way ANOVA followed by Tukey's multiple comparison was used; two-tailed P values < 0.05 (*), <0.01 (**), 0.001 (***), and <0.0001 (****). Only statistically significant differences are indicated in all panels.

cell-derived microparticles (Hartl et al., 2021; Serpas et al., 2019).

Whereas DNASE1L3 and DNASE1 comprise the majority of DNase activity in circulation (Napirei et al., 2009), the role of DNASE1 is poorly understood. Although a null mutation in DNASE1 was found in two SLE patients (Yasutomo et al., 2001), subsequent studies failed to identify this or any other deleterious *DNASE1* mutations in human SLE. Similarly, it remains controversial whether *Dnase1*-deficient mice develop SLE-like disease (Kenny et al., 2019; Napirei et al., 2006; Napirei et al., 2000). It was proposed that DNASE1 may serve to digest neutrophil extracellular traps (NETs; Hakkim et al., 2010), the genomic DNA fragments that are released by activated neutrophils during infections and inflammatory conditions (Brinkmann et al., 2004). Mice deficient in DNASE1 and DNASE1L3, but not in either enzyme alone, were shown to succumb to experimental conditions with high neutrophil numbers due to increased NET formation and NET-induced microvascular thrombosis (Jiménez-Alcázar et al., 2017). However, neither the ability of these mice to control live pathogens nor their autoimmune phenotype were examined, leaving the specific and cooperative functions of DNASE1 and DNASE1L3 unclear. Notably, both proteins are highly conserved in evolution (Mori et al., 2022; Zervou et al., 2020), suggesting a yet unknown ancestral function.

Apart from self-DNA, DNA derived from microbes promotes their infection of the mammalian hosts and thus may represent a potential target of secreted DNases. In particular, many bacterial pathogens rely on eDNA-rich biofilms to establish and maintain active infections (Flemming et al., 2016). Biofilms are commonly described as sessile microbial communities in which cells are attached to other cells or a surface and embedded in a protective polymeric matrix (Sauer et al., 2022). *Staphylococcus aureus* is one such bacterium that employs biofilms to support its pathogenic lifestyle (Lister and Horswill, 2014). *S. aureus* is a Gram-positive opportunistic pathogen that asymptomatically colonizes ~30% of the population (Wertheim et al., 2005). However, the spread of bacteria from innocuous locations in the skin and nares to peripheral tissues and organs can result in a wide array of pathologies including skin and soft tissue infections, endocarditis, pneumonia, and bloodstream infections (Thomer et al., 2016). The emergence of antibiotic-resistant forms, such as methicillin-resistant *S. aureus* (MRSA), has made the treatment of *S. aureus* infection difficult and created the need for new targeted therapies against this pathogen (Thomsen and Liu, 2018). As *S. aureus* biofilms develop, they produce an extracellular polymeric matrix composed of eDNA, polysaccharide, lysis-derived proteins, and host factors (Cue et al., 2012; Foster et al., 2014; Montanaro et al., 2011). The eDNA is thought to be derived

primarily from bacteria (Rice et al., 2007), although the contribution of host DNA has been described (Walker et al., 2005). Due to its negative charge, eDNA acts as an electrostatic polymer that can anchor bacteria to other bacteria and host factors (Lister and Horswill, 2014). Whereas recombinant DNASE1 was shown to disrupt *S. aureus* biofilm formation in vitro (Dakheel et al., 2016; Tetz et al., 2009), its impact on preformed biofilms has shown conflicting results (Houston et al., 2011; Kaplan et al., 2012), and the role of endogenous DNASE1 or other secreted DNases in bacterial infections has not been investigated in vivo.

Here, we investigated the roles of murine DNASE1 and DNASE1L3 in autoimmunity and the immune response to biofilm-forming *S. aureus*. We found that DNASE1 does not contribute to the tolerance to self-DNA yet cooperates with DNASE1L3 to control systemic infection with *S. aureus*. The two DNases were required to restrict bacterial growth and biofilm formation in the kidneys, whereas the administration of recombinant DNASE1 facilitated the clearance of biofilms and animal survival. These studies elucidate the evolutionary role of mammalian-secreted DNases in the digestion of pathogen-derived DNA and resistance to infection.

Results

DNASE1 is dispensable for immunological tolerance to self-DNA

To test the potential role of DNASE1 in immunological tolerance, we assessed the autoimmune phenotype in *Dnase1*-deficient ($D1^{-/-}$) mice and compared it with the SLE-like disease that develops in *Dnase1l3*-deficient ($D1L3^{-/-}$) mice (Sisirak et al., 2016). All mice were on the pure C57BL/6 (B6) genetic background. To test the potential redundancy between the two DNases, we also generated and analyzed *Dnase1/Dnase1l3*-double-deficient ($D1^{-/-}D1L3^{-/-}$) mice. We first assessed autoantibodies (auto-Abs) to dsDNA and nucleosomes by ELISA in these mice. $D1L3^{-/-}$ mice on C57BL/6 background progressively develop anti-dsDNA and anti-nucleosome auto-Abs starting at ∼3 mo of age (Sisirak et al., 2016). We observed the same pattern in our current cohort of $D1L3^{-/-}$ mice as well as in $D1^{-/-}D1L3^{-/-}$ mice (Fig. 1 A). In contrast, $D1^{-/-}$ mice did not develop any detectable auto-Abs at any age (Fig. 1 A). Comparing $D1L3^{-/-}$ mice to $D1^{-/-}D1L3^{-/-}$ mice, we did not observe any significant increase in autoantibody titers or acceleration of their development. Similarly, only $D1L3^{-/-}$ but not $D1^{-/-}$ mice accumulated splenic antibody-secreting cells reactive to dsDNA and nucleosomes by 1 yr of age, and their frequency was not increased in $D1^{-/-}D1L3^{-/-}$ compared with $D1L3^{-/-}$ mice (Fig. 1, B and C).

Sca-1 is a GPI-anchored cell surface protein of unknown function, the expression of which is upregulated on lymphocytes by type I IFN and thus represents a sensitive flow cytometry–based readout of the aberrant IFN signaling in SLE models (Lee et al., 2008). Indeed, *Dnase1l3*-deficient mice show progressive upregulation of Sca-1 that reflects the ongoing pathogenic type I IFN response (Soni et al., 2020). Splenic $CD4^+$ T cells from $D1L3^{-/-}$ mice showed significantly higher levels of Sca-1 compared with WT and $D1^{-/-}$ mice at 1 yr of age, and no further increase was detected in $D1^{-/-}D1L3^{-/-}$ mice (Fig. 1 D). Finally, $D1L3^{-/-}$ but not $D1^{-/-}$ mice at 1 yr showed swelling of kidney glomeruli (indicative of antibody-mediated kidney damage), and no further increase was observed in $D1^{-/-}D1L3^{-/-}$ mice (Fig. 1 E). Collectively, these data suggest that the loss of DNASE1 does not cause autoreactivity to DNA by itself and does not amplify the loss of DNASE1L3. Thus, only DNASE1L3 is uniquely and non-redundantly required for tolerance to self-DNA, leaving open the question of the biological role of DNASE1.

DNASE1 and DNASE1L3 are required for the control of systemic *S. aureus* infection

Given that many nucleases are directly involved in antimicrobial responses and that DNASE1-like nucleases are conserved in vertebrate evolution, we hypothesized that DNASE1 and/or DNASE1L3 might facilitate immunity to infection. We therefore examined their role in the control of bloodstream infection with *S. aureus*, a common cause of bacteremia and sepsis. $D1^{-/-}$, $D1L3^{-/-}$, and $D1^{-/-}D1L3^{-/-}$ mice were infected i.v. (1×10^7 CFU/mouse) with USA300 strain LAC, a prototypic community-acquired MRSA strain (Thurlow et al., 2012). Almost all the $D1^{-/-}D1L3^{-/-}$ mice succumbed to infection within 72 h (as defined by weight loss >20%), a significant decrease compared to only 44% of WT mice at that point (Fig. 2 A). The survival of $D1L3^{-/-}$ mice was comparable with WT mice, while $D1^{-/-}$ mice showed an intermediate survival that was not significantly reduced compared with WT mice (Fig. 2 A). A reduction of the bacterial inoculum by 30% or less can improve the survival rate in this model (Tam et al., 2020). We, therefore, infected mice with a lower dose of MRSA (7.5×10^6 CFU/mouse), which resulted in a complete survival of WT mice (Fig. 2 B). In contrast, >50% $D1^{-/-}D1L3^{-/-}$ succumbed to infection, confirming their increased susceptibility. Accordingly, at 72 h after infection, the bacterial burden was significantly increased in the lung, liver, spleen, heart, and kidneys of $D1^{-/-}D1L3^{-/-}$ mice compared with WT mice (Fig. 2 C). Notably, the bacterial burden in kidneys exceeded 10^6 CFU/mg compared with $<10^3$ CFU/mg in other tissues, highlighting the kidney as the major site of tissue inflammation in this model as described previously (Cheng et al., 2011; Kim et al., 2014; Thomer et al., 2016). $D1^{-/-}$ mice showed elevated bacterial burden only in the liver, while $D1L3^{-/-}$ mice were similar to WT mice (Fig. 2 C). Thus, in the context of systemic *S. aureus* infection, the loss of DNASE1L3 had no effect and the loss of DNASE1 partially impaired resistance, whereas the combined loss of both DNASE1 and DNASE1L3 rendered mice highly susceptible, suggesting that both DNases facilitate antibacterial immunity in a synergistic manner.

To understand why $D1^{-/-}D1L3^{-/-}$ mice succumbed to infection, we analyzed lungs, livers, hearts, and kidneys of infected mice by histology. At 18 h after infection, no overt pathology was observed in any organ of $D1^{-/-}D1L3^{-/-}$ mice when compared with uninfected WT mice (Fig. S1, A and B). As animal survival was defined by weight loss and clinical symptoms, the majority of mice (including those designated as non-surviving) at 72 h after infection were available for tissue harvesting. At this point, no significant pathology was observed in the liver, lungs, or heart of mice of any genotype (Fig. S1, C–H). In contrast, significant renal pathology was observed in all groups at the 72-h

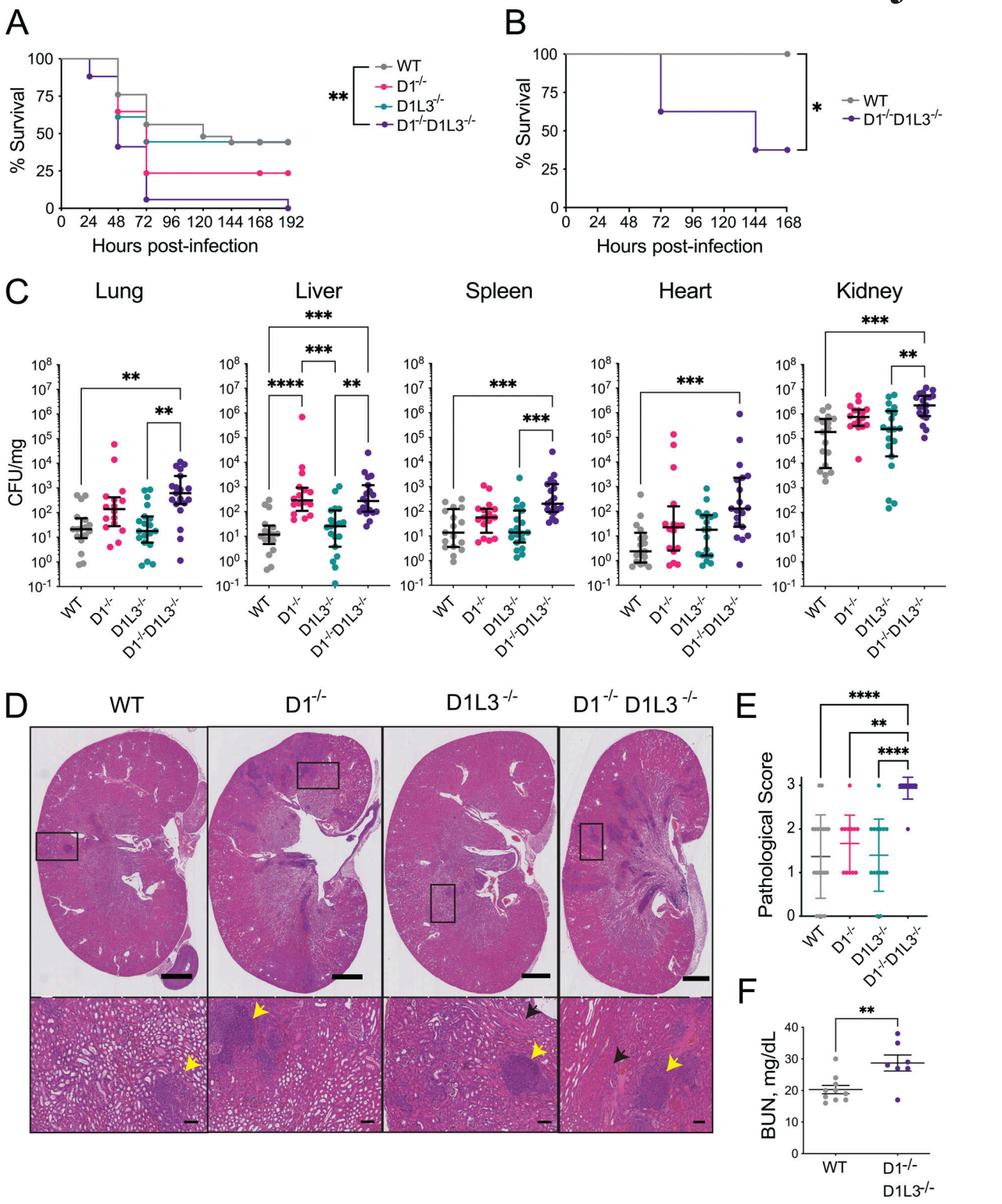

Figure 2. **Deficiency of DNASE1 and DNASE1L3 impairs control of systemic *S. aureus* infection. (A)** Survival of mice of indicated genotypes that were infected i.v. with 1×10^7 CFU of *S. aureus* (n = 17–25 mice per group, pooled from three separate experiments). **(B)** Survival of mice of indicated genotypes that were infected i.v. with 7.5×10^6 CFU of *S. aureus* (n = 7–8 mice per group). **(C)** Bacterial burden in the indicated organs of mice infected as in A and sacrificed 72 h later. Symbols represent individual mice; bars represent the median ± interquartile range of 16–19 mice per group; data are shown on a log scale. **(D and E)** Kidney pathology in the infected mice 72 h after infection. **(D)** H&E-stained sections of kidneys (representative of at least 12 mice per group). Scale bars, 1 mm (whole kidney) and 100 µm (magnified image). Arrows indicate areas of immune cell infiltration (yellow) and tissue necrosis (black). **(E)** Pathological scoring for the kidneys from indicated genotypes. Symbols represent individual mice; bars represent mean ± SD of 12–19 mice per group. **(F)** Blood urea nitrogen (BUN) in the blood of infected mice 72 h after infection. Symbols represent individual mice, bars represent mean ± SD of 7–10 mice per group. Statistical significance between groups was determined by log-rank (Mantel–Cox) test (A and B) using Bonferroni correction for multiple comparisons where appropriate (A), Kruskal–Wallis test followed by the Dunn's multiple-comparison test (C and E), or Student's t test (F). Two-tailed P values <0.01 (**), <0.001 (***), and <0.0001 (****); Bonferroni corrected two-tailed P value <0.017 (**). Only significant differences are indicated in all panels.

time point, including abscesses, immune infiltrates, and tissue necrosis (Fig. 2 D), consistent with the kidney being a preferred target of *S. aureus* in this model. Notably, the pathology was significantly more severe in D1$^{-/-}$D1L3$^{-/-}$ mice compared with WT, D1$^{-/-}$, or D1L3$^{-/-}$ mice (Fig. 2, D and E). The pathology could be observed throughout all kidney areas and coincided with the presence of Gram-positive staphylococci (Fig. S2). Accordingly, biochemical analysis of serum showed elevated levels of blood urea nitrogen in infected D1$^{-/-}$D1L3$^{-/-}$ compared with WT mice, which is indicative of renal dysfunction (Fig. 2 F). Although the contribution of other organ pathology cannot be ruled out, the observed high bacterial burdens, severe tissue inflammation, and impaired function suggest kidney pathology as the main driver of the increased susceptibility of D1$^{-/-}$D1L3$^{-/-}$ mice to *S. aureus*–mediated bloodstream infection.

DNASE1 and DNASE1L3 do not control NET formation or cytokine response to *S. aureus* infection

To investigate the mechanism behind the enhanced kidney pathology and bacterial growth in D1$^{-/-}$D1L3$^{-/-}$ mice, we focused on the innate immune system that is essential for the control of *S. aureus* infection. We assessed 13 inflammatory mediators in the plasma of WT, D1$^{-/-}$, D1L3$^{-/-}$, and D1$^{-/-}$D1L3$^{-/-}$ mice 18 and 72 h following *S. aureus* infection. The majority of cytokines including IL-1α, IL-1β, IL-12p70, IL-17A, IL-23, IL-27, IFN-β, IFN-γ, and GM-CSF showed no differences between experimental groups (data not shown). The only observed differences in D1$^{-/-}$D1L3$^{-/-}$ mice included modest increases in IL-6 (at 18 h; Fig. 3 A) and TNF-α and IL-10 (at 72 h; Fig. 3, B and C). Importantly, no cytokine was significantly decreased in D1$^{-/-}$D1L3$^{-/-}$ mice, although there was a trend toward lower CCL2 at 18 h (Fig. 3 D). We also assessed immune populations in the blood and kidneys 72 h after infection. As expected, all infected mice showed a dramatic increase in neutrophil frequencies (Fig. 3, E and F) and absolute numbers (Fig. 3 G) compared with uninfected mice. Notably, the influx of neutrophils in both blood and kidneys was significantly higher in D1$^{-/-}$D1L3$^{-/-}$ mice compared with WT controls (Fig. 3, E–G). In contrast, Ly-6C^{hi} inflammatory monocytes (Kratofil et al., 2017) were increased in all infected mice but showed no significant differences between the groups (data not shown). The observed increase in cytokine response and neutrophil recruitment in D1$^{-/-}$D1L3$^{-/-}$ mice likely reflects their elevated bacterial burden and argues against a defect in the innate immune response to infection.

It has been reported that D1$^{-/-}$D1L3$^{-/-}$ mice exhibit uniform mortality following cytokine- or bacterial product-induced neutrophilia due to defective clearance of NETs and the resulting NET-mediated blood clotting in the lungs (Jiménez-Alcázar et al., 2017). Given the increased neutrophil numbers in *S. aureus*–infected D1$^{-/-}$D1L3$^{-/-}$ mice, we tested if excessive NETosis might contribute to the resulting pathology. NETs were quantified in the plasma of infected mice using ELISA, which detects myeloperoxidase-DNA complexes characteristic of NETs. In contrast to the robust detection of myeloperoxidase-DNA in the bronchoalveolar lavage fluid from neutrophil-infiltrated mouse lungs (positive control), no NETs were detected in the plasma of infected mice at 18 or 72 h (Fig. 3 H). To further rule out the role of NETs, we treated mice according to Jiménez-Alcázar et al. (2017) with three consecutive i.p. injections of LPS every 24 h followed by a single i.v. injection of heat-killed *Escherichia coli*. In both WT and D1$^{-/-}$D1L3$^{-/-}$ mice, this treatment caused a major influx of neutrophils in the blood (Fig. S3 A) and broad induction of ICAM-1 and Sca-1 expression (Basit et al., 2006; Shi et al., 2013) 24 h later (Fig. S3, B and C). The induced neutrophilia was comparable with that observed after *S. aureus* infection (Fig. S3 D); furthermore, the LPS/*E. coli* treatment caused additional pathology including splenomegaly, anemia, and thrombocytopenia (Fig. S3, E–H). Notwithstanding these severe effects, D1$^{-/-}$D1L3$^{-/-}$ mice showed no increased weight loss (Fig. 3 I), a non-significant decrease in survival (Fig. 3 J), and no blood clots or other abnormalities in the lungs at either 24 or 40 h following *E. coli* injection (Fig. 3 K). These results do not support the proposed excessive NETosis in D1$^{-/-}$D1L3$^{-/-}$ mice and argue against the latter as a mechanism for increased susceptibility to *S. aureus* infection.

DNASE1 and DNASE1L3 prevent the formation of bacterial biofilm in the kidney

Biofilms provide a protective niche that shields bacteria from the immune system and facilitates bacterial outgrowth and pathogenicity (Flemming et al., 2016). Bacterial biofilms are composed of a mixture of bacterial proteins, bacterial cell components, and DNA (Zapotoczna et al., 2016) and therefore can be thought of as a type of eDNA substrate. As such, we hypothesized that the increased susceptibility of D1$^{-/-}$D1L3$^{-/-}$ mice to *S. aureus* might be due to their inability to digest bacterial DNA and disperse biofilms.

To test this notion, we first analyzed the kidneys of *S. aureus*–infected mice by electron microscopy (EM). Transmission EM revealed the presence of characteristic bacterial cell structures within the kidney inflammatory lesions of D1$^{-/-}$D1L3$^{-/-}$ mice at 72 h after infection (Fig. S4), as confirmed through the depth of the lesion by serial block-face scanning EM (Video 1). Scanning EM revealed very few bacterial aggregates in the kidneys of infected WT mice compared with uninfected controls (Fig. 4, A and B). In contrast, the kidneys of D1$^{-/-}$D1L3$^{-/-}$ mice harbored extensive bacterial aggregates (Fig. 4 C), in which tight clusters of planktonic *S. aureus* (colorized in purple) were surrounded by biofilm-like structures comprising bacteria and extracellular matrix (colorized in yellow). To detect and quantify DNA-containing bacterial lesions, we stained kidneys of infected mice by immunohistochemistry with an antibody against *S. aureus* and with DAPI to visualize DNA by immunofluorescence. We found that the rare bacterial lesions in the kidneys of WT mice at 72 h after infection showed dense DAPI staining (Fig. 4 D). The lesions were similarly DAPI-positive in the kidneys of D1$^{-/-}$D1L3$^{-/-}$ mice (Fig. 4 E) but were more frequent and occupied a significantly larger area (Fig. 4 F). Similar results were obtained at an earlier time point of 48 h after infection, when the majority of WT mice had no bacterial lesions in the kidneys (Fig. S5, A–C).

We tested whether the DNA-rich bacterial foci in the kidney contain bacterial eDNA and thus represent a biofilm. Staining with DAPI was insufficient for this purpose because it equally

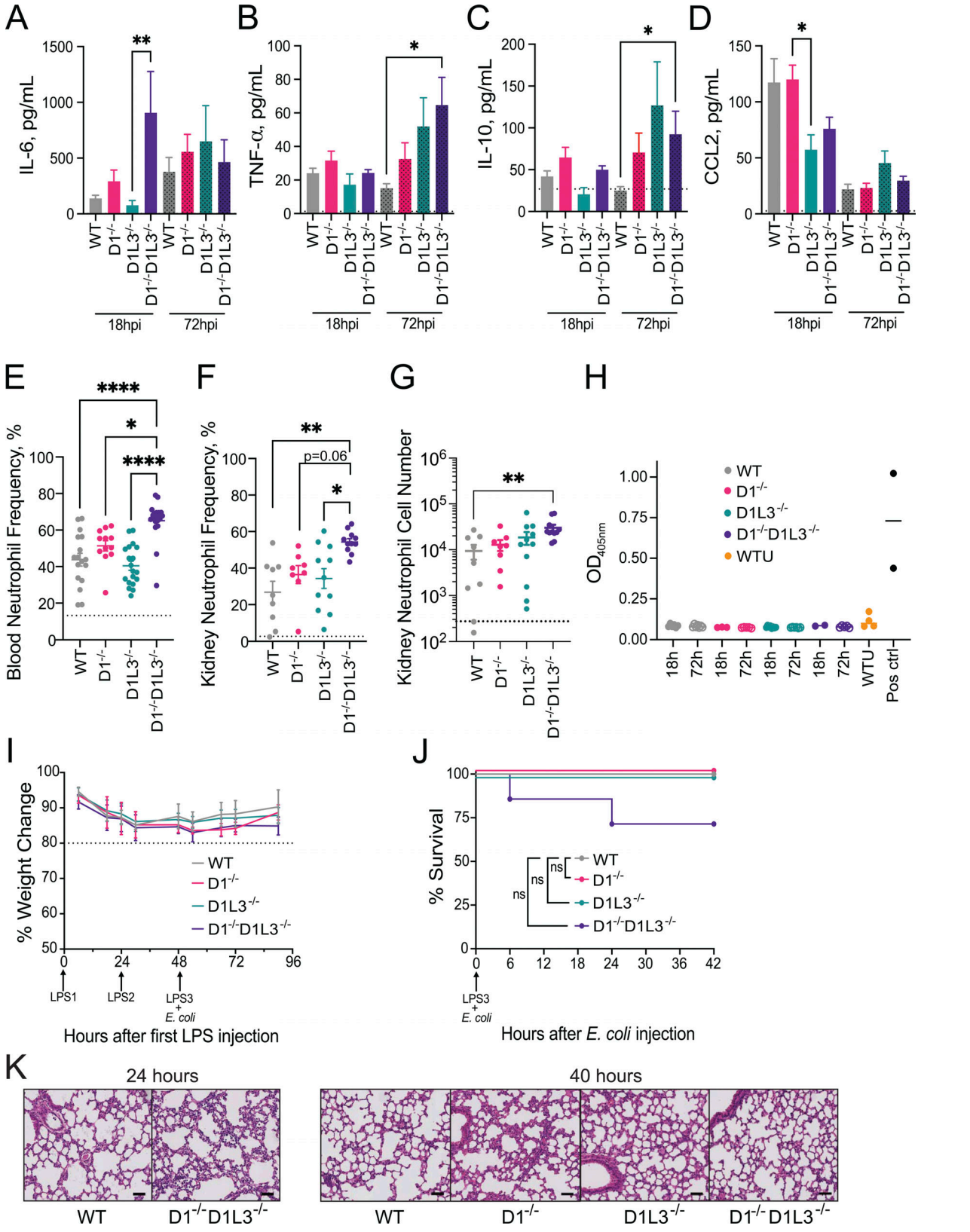

Figure 3. **Deficiency of DNASE1 and DNASE1L3 does not affect NETosis or cytokine response to bacteria.** Mice of the indicated genotypes were infected i.v. with 1 × 10^7 CFU of *S. aureus* and sacrificed 18 or 72 h later. **(A–D)** Levels of the indicated cytokines in the plasma. Bars represent mean ± SEM of n = 5–9 mice per group; dotted lines represent levels in uninfected WT mice. **(E–G)** Frequency of neutrophils among total single cells in the blood (E) and kidneys (F), and absolute numbers of neutrophils in the kidneys (G) 72 h after infection. Symbols represent individual mice; bars represent mean ± SEM of 9–11 mice per group; dotted lines represent levels in uninfected WT mice. **(H)** Detection of NETs in the plasma of infected mice using ELISA for myeloperoxidase-DNA

complexes. Symbols represent individual mice; bars represent the median of two to eight mice per group; bronchoalveolar lavage fluid from mice with lung neutrophilia was used as a positive control (Pos ctrl). **(I–K)** Mice of indicated genotypes were given two daily doses of LPS (LPS-1, LPS-2) and one dose of LPS with heat-killed *E. coli* (LPS-3+*E. coli*). **(I)** Animal weights during the experiment. Data represent mean ± SD of 7–10 mice per group; dotted line indicates the 20% weight loss cutoff used for endpoint criteria. **(J)** Animals were monitored for survival after the last injection based on >20% weight loss or signs of distress. **(K)** H&E-stained sections of lungs at 24 h or 40 h following LPS + *E. coli* injection. Images are representative of at least seven mice per group. Scale bars, 50 µm. Statistical significance was determined by Kruskal–Wallis test followed by Dunn's multiple-comparison test for comparisons between genotypes at the same time point (A–G). Two-tailed P values <0.05 (*), <0.01 (**), <0.0001 (****); ns, not significant. Only significant differences are indicated in A–G.

stains both bacterial and host DNA. To distinguish between bacteria-derived DNA and mouse-derived DNA, we stained for 5-methylcytosine (5-mC), which is very common in mammalian DNA as part of the methylated *CpG* motif. In contrast, 5-mC in bacteria is present only in certain restriction enzyme sites modified by the *Dcm* methylase (Sánchez-Romero et al., 2015), which is absent in *S. aureus* (Dreiseikelmann and Wackernagel, 1981). In WT mice, the majority of the *S. aureus*–containing areas that were positive for DAPI were also positive for 5-mC (Fig. 5, A and B), suggesting the abundance of host DNA. Some DAPI-positive areas with low or negative 5-mC staining were also observed, likely reflecting the occasional formation of biofilms with high bacterial DNA content. In contrast, nearly all *S. aureus*–containing DAPI-positive lesions in D1$^{-/-}$D1L3$^{-/-}$ kidneys were low or negative for 5-mC (Fig. 5, C and D). To quantify the eDNA area while normalizing for the number of bacterial lesions, we calculated the area of strong DAPI staining as DNA from both bacteria and host and subtracted the 5-mC–positive area as DNA from the host. This analysis indicated that only three out of eight WT mice harbored small (<1 mm^2) detectable areas of microbial eDNA, whereas all eight D1$^{-/-}$D1L3$^{-/-}$ mice contained larger (>1 mm^2) areas (Fig. 5 E). Similar results were also observed at the earlier 48 h time point (Fig. S5, D–F). The specificity of 5-mC staining was confirmed by the absence of signal in *S. aureus* biofilms formed in vitro, in contrast to the positive staining of mammalian cell nuclei (Fig. 5 F).

We sought to further confirm that the observed lesions enriched in bacterial eDNA represent biofilms. Biofilm formation by methicillin-resistant staphylococci requires wall teichoic acid (WTA; Mann et al., 2016), which is detected by a recently developed anti-WTA mAb (de Vor et al., 2022). While this mAb is not completely specific for the biofilm vs. planktonic forms, it allows faithful detection of *S. aureus* biofilm in vivo. This mAb weakly stained small *S. aureus* lesions in the kidneys of WT mice, likely reflecting the expected low-level biofilm formation in these lesions (data not shown). Importantly, it showed strong staining of *S. aureus* lesions in the kidneys of D1$^{-/-}$D1L3$^{-/-}$ mice (Fig. 6, A–D), consistent with large-scale biofilm formation. Next, we tested the hallmark effect of biofilm formation, i.e., increased resistance to antibiotics. We found that the treatment of *S. aureus*–infected animals with vancomycin rescued the survival of WT mice (Fig. 6 E) but not of D1$^{-/-}$D1L3$^{-/-}$ mice (Fig. 6 F). Note that the slightly improved survival of D1$^{-/-}$D1L3$^{-/-}$ mice in these experiments compared with Fig. 2 A may reflect experimental variables such as the injection of PBS (as a vehicle or containing vancomycin) at 24 h after infection. Collectively, these results suggest that the absence of secreted DNases facilitates the formation of eDNA-rich drug-resistant biofilms in the kidneys of *S. aureus*–infected mice.

S. aureus is known to form abscesses in the kidneys of i.v. infected animals, in which the staphylococci are surrounded by layers of phagocytes (Cheng et al., 2011; Thammavongsa et al., 2013). Amongst phagocytes, the recruitment of neutrophils is critical for the containment of *S. aureus* infection (Robertson et al., 2008). Indeed, staining of kidney sections for the neutrophil marker Ly-6G revealed extensive neutrophil infiltration into the DAPI-positive bacterial lesions in WT mice at 72 h after infection (Fig. 7, A and B). In contrast, many DAPI-positive lesions in D1$^{-/-}$D1L3$^{-/-}$ kidneys were surrounded but not infiltrated by neutrophils (Fig. 7, C and D), as also observed 48 h after infection (Fig. S5, G and H). The total Ly-6G$^+$ area was increased in D1$^{-/-}$D1L3$^{-/-}$ kidneys due to more extensive bacterial lesions (Fig. 7 E). However, the fraction of Ly-6G–negative areas within DAPI$^+$ lesions (i.e., bacterial lesions not infiltrated by neutrophils) was also significantly increased (Fig. 7 F). Collectively, these results suggest that the susceptibility of D1$^{-/-}$D1L3$^{-/-}$ mice to infection is due to increased biofilm formation and the resulting inability of neutrophils to eliminate *S. aureus* in the kidney.

Treatment with DNASE1 ameliorates *S. aureus* infection in vivo by disrupting biofilms

Given that DNASE-deficient mice are unable to control biofilm formation by *S. aureus*, we tested whether therapeutic delivery of a secreted DNASE would improve biofilm dispersal and infection control. First, we confirmed previous data (Kaplan et al., 2012; Tetz et al., 2009) that DNASE1 was able to disperse in vitro–generated biofilms over a wide range of concentrations (Fig. 8 A). Similarly, we found that DNASE1L3 was also able to disperse in vitro–generated biofilms, with no additive effect observed between the two enzymes (Fig. 8 A). To extend these studies in vivo, we took advantage of Dornase alfa (Pulmozyme, hereafter Dornase), a therapeutic formulation of human DNASE1 used as an inhalant to loosen the mucus of patients with cystic fibrosis (Yang and Montgomery, 2021). First, we tested the ability of Dornase to rescue the phenotype of D1$^{-/-}$D1L3$^{-/-}$ mice by infecting them with *S. aureus* and administering Dornase i.v. 4 h after infection and then daily for 4 d. Whereas all buffer-treated mice succumbed to the infection as expected, the majority of Dornase-treated mice survived (Fig. 8 B). Next, we tested whether similar systemic treatment with Dornase could improve the survival of WT mice. Indeed, WT mice treated with Dornase exhibited improved survival (Fig. 8 C) and reduced bacterial burdens in the kidney (Fig. 8 D) and liver (Fig. 8 E) at 96 h after infection. Staining of kidneys revealed that Dornase treatment also reduced the area of *S. aureus* lesions (Fig. 8 F), the area of DAPI$^+$ 5-mC$^-$ bacterial biofilm (Fig. 8 G), and the area of DAPI$^+$ lesions not infiltrated by Ly-6G$^+$ neutrophils (Fig. 8 H).

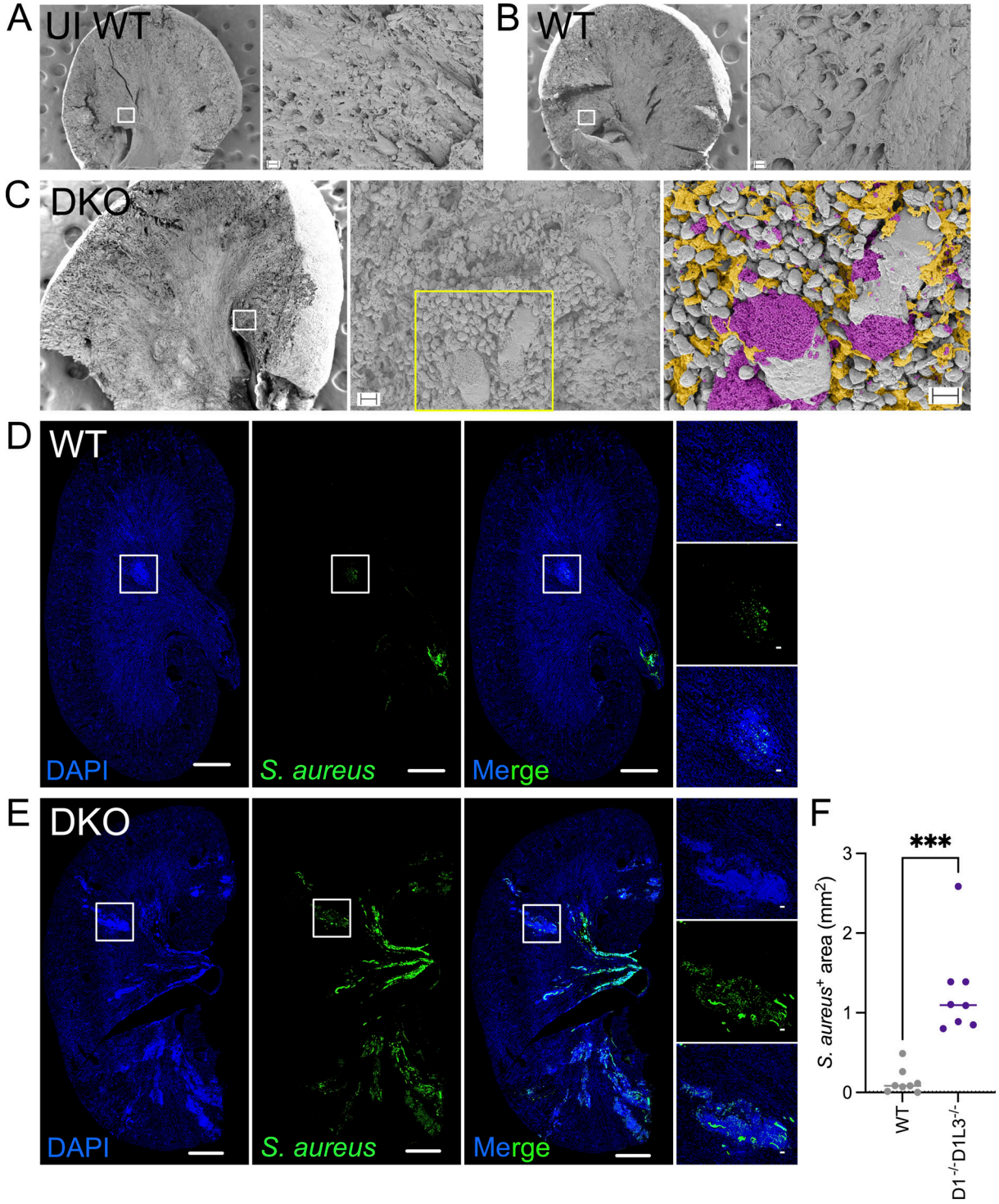

Figure 4. **Deficiency of DNASE1 and DNASE1L3 promotes DNA-containing bacterial lesions in the kidney.** WT or D1$^{-/-}$D1L3$^{-/-}$ double-knockout (DKO) mice were infected i.v. with 1 × 10^7 CFU of *S. aureus*, and their kidneys were examined 72 h later. **(A–C)** Scanning EM of kidney tissue from uninfected (UI) WT mice (A), infected WT mice (B), and infected DKO mice (C). Shown are low-magnification images of the kidney and magnified images of areas in white boxes (scale bars, 10 µm). An additional magnified image of the bacterial lesion in DKO mice (yellow box) is shown with pseudocolored clusters of planctonic *S. aureus* (purple) and biofilm-like structures comprised of bacteria and extracellular matrix (yellow). Representative of 10–12 magnified areas per kidney from two mice per condition/genotype. **(D and E)** Immunohistochemistry of kidney sections from infected WT (D) and DKO (E) mice stained with anti–*S. aureus* antibody and DAPI. Shown are low magnification (4×) images of the entire kidney (scale bar, 1 mm) and magnified images of areas in white boxes (scale bars, 50 µm). The images are representative of eight mice per genotype analyzed in two independent experiments. **(F)** Quantification of *S. aureus*–positive area in kidney sections. Symbols represent individual mice; bars represent median. Dotted line represents the mean value of uninfected WT mice. Statistical significance was determined by Mann–Whitney test; two-tailed P value < 0.001 (***).

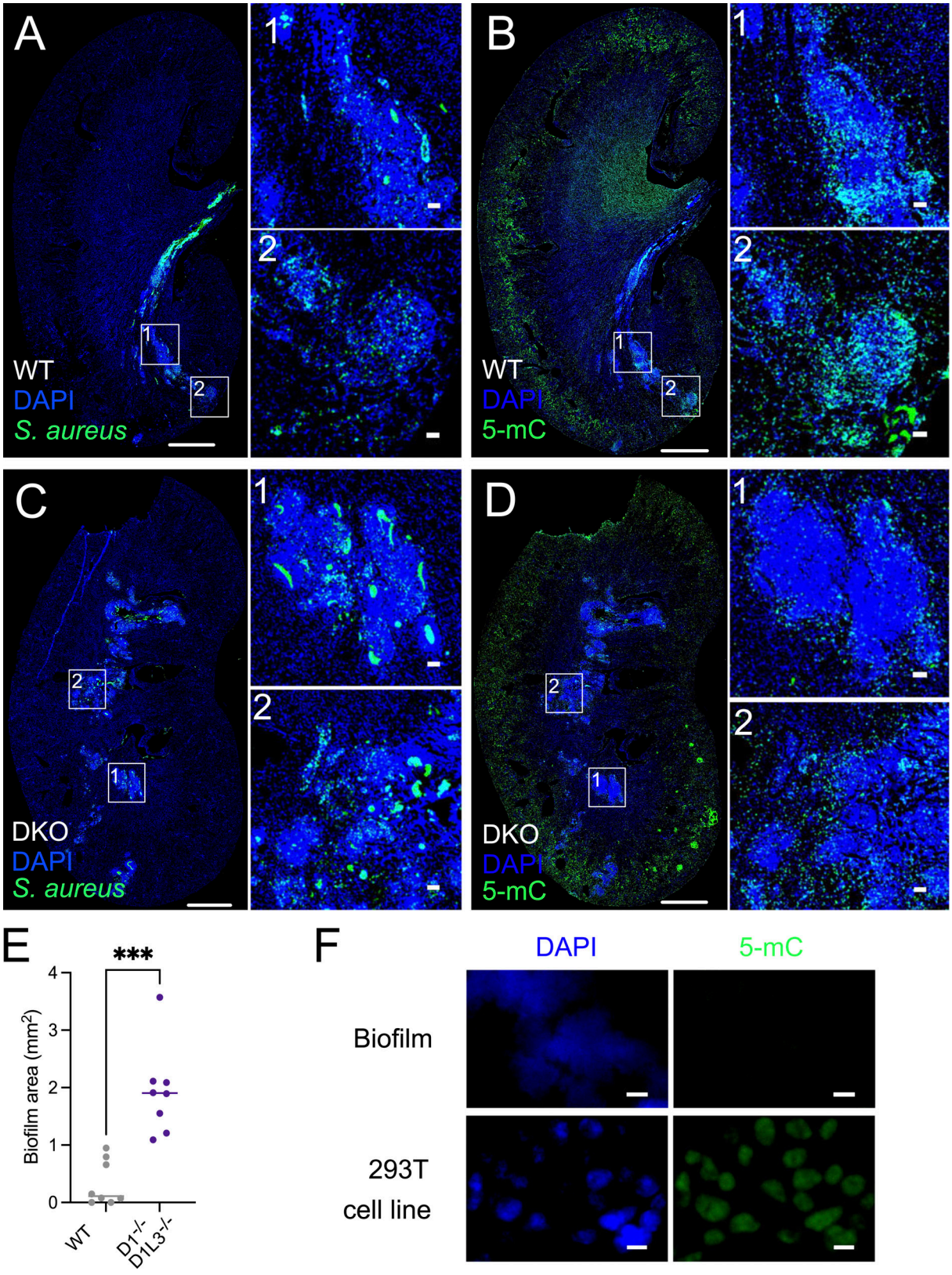

Figure 5. **Deficiency of DNASE1 and DNASE1L3 promotes bacterial biofilm formation in the kidney.** WT or D1$^{-/-}$D1L3$^{-/-}$ DKO mice were infected i.v. with 1 × 10^7 CFU of *S. aureus*, and their kidneys were examined by immunohistochemistry 72 h later. **(A–D)** Shown are serial sections of WT (A and B) and DKO (C and D) kidneys stained with DAPI and antibodies to *S. aureus* (A and C) or 5-mC (B and D). Each panel includes low-magnification images of the entire kidney (scale bar, 1 mm) and magnified images of areas in white boxes (scale bars, 50 µm). Representative of eight mice per genotype. **(E)** Quantification of DAPI-positive 5-mC–negative biofilm area in kidney sections. Symbols represent individual mice; bars represent the median. **(F)** *S. aureus* biofilms or cultured mammalian 293T cells were stained with DAPI and antibodies to 5-mC (scale bar, 10 µm). Representative of two experiments. Statistical significance was determined by Mann–Whitney test; two-tailed P value < 0.001 (***).

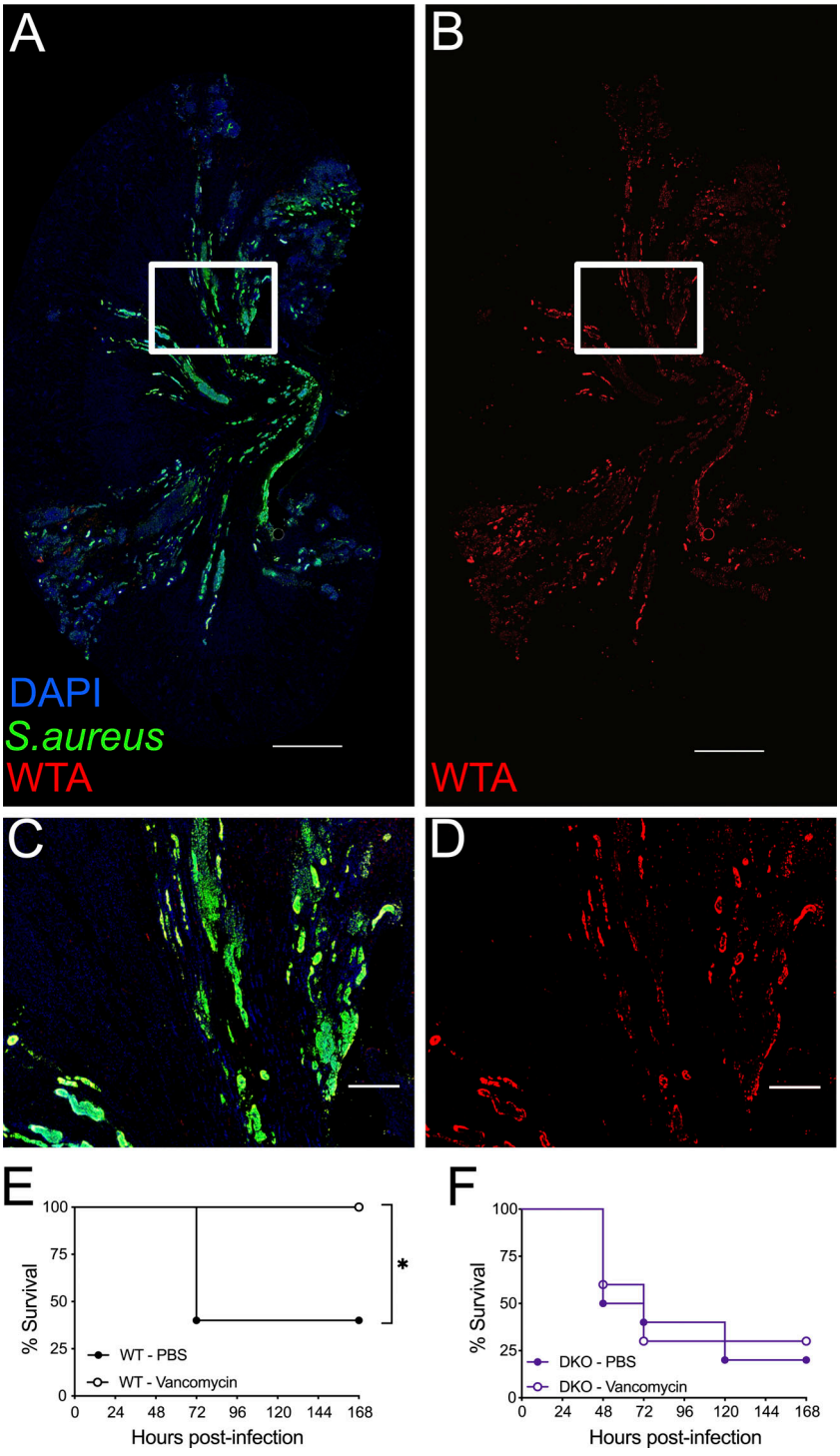

Figure 6. **Bacterial lesions in the kidneys of DNase-deficient mice are positive for biofilm staining and confer resistance to antibiotics.** $D1^{-/-}D1L3^{-/-}$ DKO mice were infected i.v. with 1×10^7 CFU of *S. aureus*, and their kidneys were examined by immunohistochemistry 72 h later. **(A–D)** Sections of DKO mice were stained with DAPI, antibodies to *S. aureus*, and anti-WTA antibody that detects biofilms in vivo. Shown are low-magnification images of the entire kidney (A and B; scale bar, 1 mm) and magnified images of boxed areas (C and D; scale bars, 250 µm). Representative of four samples; no staining was observed with an isotype control for anti-WTA (data not shown). **(E and F)** Survival of mice that were infected i.v. with 1×10^7 CFU of *S. aureus* and injected s.c. with vancomycin or PBS 24 h later. **(E)** WT mice, $n = 5$ per treatment group. **(F)** DKO mice, $n = 10$ per treatment group. Statistical significance between groups was determined by log-rank (Mantel–Cox) test. Two-tailed P values <0.05 (*).

These differences were statistically significant, except for the reduction of Ly-$6G^+$ area (Fig. 8, I–L). Altogether, these findings confirm the ability of secreted DNases to control *S. aureus* infection by digesting biofilms and implicate them as potential therapeutic agents.

Discussion

Our study aimed to define the physiological roles of secreted mammalian DNase proteins of the DNase I family. Among its four members, DNASE1L1 is a glycosylphosphatidyl inositol–anchored cell surface protein of unknown function (Shiokawa et al., 2007), whereas DNASE1L2 is expressed primarily in the skin and facilitates DNA removal from skin appendages (Fischer et al., 2011). DNASE1 and DNASE1L3 are homologous secreted DNases, yet only DNASE1L3 has been firmly established to prevent autoreactivity to DNA, whereas the role of DNASE1 remains controversial. We found that the deficiency of DNASE1 on pure C57BL/6 background neither caused anti-nucleosome or anti-DNA antibody reactivity nor enhanced the autoimmune

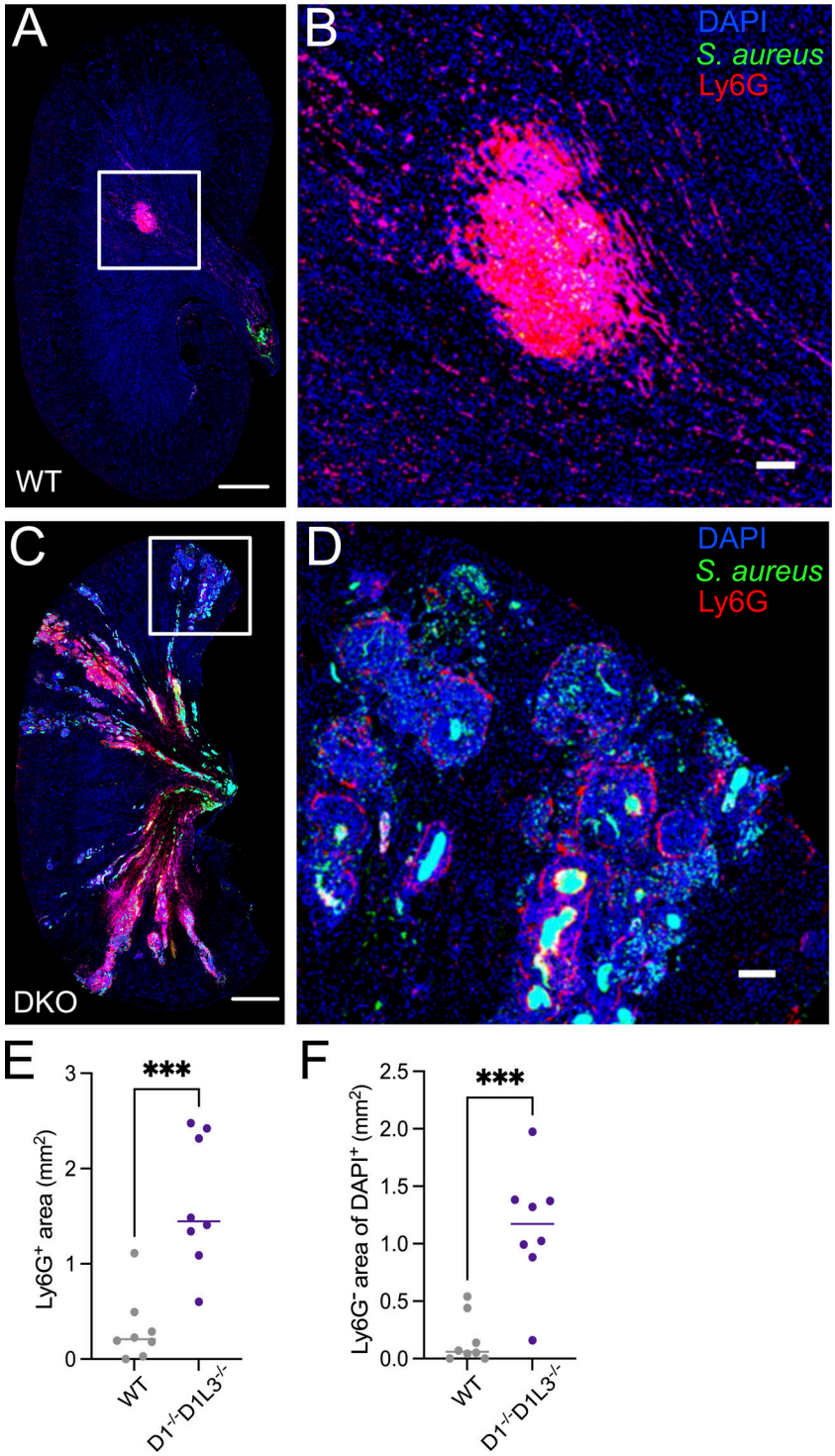

Figure 7. **Biofilm prevents the infiltration of neutrophils into bacterial lesions.** WT or $D1^{-/-}D1L3^{-/-}$ DKO mice were infected i.v. with 1×10^7 CFU of *S. aureus*, and their kidneys were examined by immunohistochemistry 72 h later. **(A–D)** Sections of WT (A and B) and DKO (C and D) mice were stained with DAPI and antibodies to *S. aureus* and Ly-6G. Shown are low-magnification images of the entire kidney (A and C; scale bar, 1 mm) and magnified images of areas in white boxes (B and D; scale bars, 50 µm). **(E and F)** Quantification of total Ly-6G–positive area (neutrophil infiltration; E) and Ly-6G–negative area within DAPI-positive lesions (neutrophil exclusion from lesions; F) in kidney sections. Symbols represent individual mice; bars represent the median. Statistical significance was determined by Mann–Whitney test; two-tailed P value < 0.001 (***).

manifestations in DNASE1L3-deficient mice. This is in contrast to the original report of SLE-like disease in DNASE1-deficient mice (Napirei et al., 2000); however, these mice were on a mixed B6/129 background, which may generate SLE-like symptoms on its own (Bygrave et al., 2004). Indeed, the SLE phenotype was no longer observed on a pure B6 background (Napirei et al., 2006). Anti-nucleosome and anti-DNA reactivity was recently reported in another *Dnase1*-deficient strain (Kenny et al., 2019); however, this study did not use DNASE1L3-deficient mice or other common SLE models as positive controls, thus the magnitude and physiological significance of the observed phenotypes are difficult to assess. Some autoreactivity to yet unknown self-antigens could not be ruled out in our DNASE1-deficient mice; thus, DNASE1 could still mitigate local kidney inflammation in SLE patients as proposed (Seredkina and Rekvig, 2011; Zykova et al., 2010). Nevertheless, our results argue against the proposed role of DNASE1 in maintaining immune tolerance to DNA (Hakkim et al., 2010; Kenny et al., 2019;

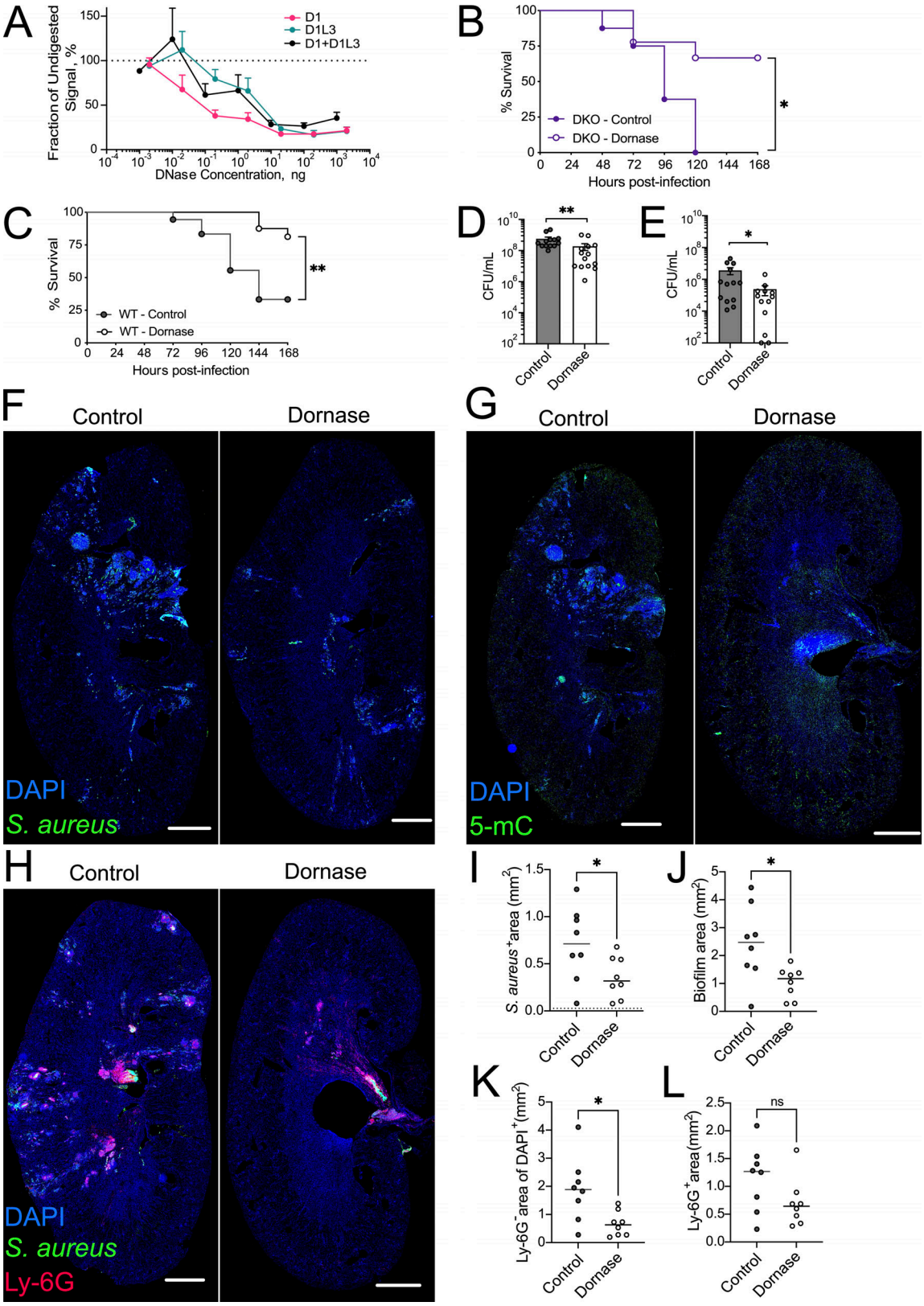

Figure 8. **Treatment with DNASE1 ameliorates *S. aureus* infection in vivo. (A)** Dispersal of biofilms by recombinant DNases. *S. aureus* biofilms were grown and digested in vitro with a concentration range of recombinant DNASE1 and DNASE1L3, and the remaining biofilm was quantified. The OD values from each experiment were normalized to the undigested OD value from that experiment and plotted as a fraction of the undigested signal; bars represent mean ± SEM. **(B–E)** Mice were infected i.v. with 1×10^7 CFU *S. aureus* and treated with Dornase or with buffer only (control) at 4, 24, 48, 72, and 96 h after infection. Mice were sacrificed at 30% weight loss for humane endpoint. **(B)** Survival of $D1^{-/-}D1L3^{-/-}$ DKO mice (n = 8–9 per group). **(C)** Survival of WT mice (n = 16–18 per

group). **(D and E)** Bacterial burden in the kidney (D) and liver (E) of infected Dornase- or buffer-treated WT mice 96 h after infection. Symbols represent individual mice; bars represent mean ± SEM. **(F–L)** WT mice were infected i.v. with 1×10^7 CFU *S. aureus* and treated with Dornase or with buffer only (control) at 4, 24, and 48 h after infection, and their kidneys were examined by immunohistochemistry 72 h after infection. **(F–H)** Representative images of whole kidney sections stained with DAPI and antibodies to *S. aureus* (F), 5-mC (G), and *S. aureus* plus Ly-6G (H). Scale bar, 1 mm. **(I–L)** Quantification of *S. aureus*–positive area (I), DAPI-positive 5-mC–negative biofilm area (J), Ly-6G–negative area within DAPI-positive lesions (K), and total Ly-6G–positive area (L) per kidney. Symbols represent individual mice; bars represent the median. The dotted line in I represents the mean value of uninfected WT mice. Statistical significance between groups was determined by log-rank (Mantel–Cox) test (B and C) and Mann–Whitney test in other panels. Two-tailed P values <0.05 (*) and <0.01 (**); ns, not significant.

Yasutomo et al., 2001) and highlight a unique role of DNASE1L3 in the clearance of immunogenic self-DNA and prevention of systemic autoimmunity.

DNASE1 and DNASE1L3 are highly conserved in evolution, suggesting that they have an ancestral function that predates protection from autoantibody responses. Moreover, DNASE1L3 is expressed primarily in innate immune cells such as dendritic cells and macrophages (Sisirak et al., 2016; Wilber et al., 2002), suggesting that its ancestral function may be related to innate immunity. We therefore tested separate and combined roles of DNASE1 and DNASE1L3 in a prototypic bacterial infection that is normally controlled by innate immunity. We found that the combined loss of both DNases made mice significantly more susceptible to systemic infection with *S. aureus*, whereas systemic administration of DNASE1 protected them from it. One possible explanation of this effect could be the proposed role of DNASE1 and DNASE1L3 in the digestion of NETs (Jiménez-Alcázar et al., 2017). NETs were shown to promote tissue injury in certain infection models, and this effect was counteracted by DNASE1: thus, local treatment with DNASE1 ameliorated lung injury in *S. aureus*–induced pneumonia (Lefrançais et al., 2018), whereas DNASE1-deficient mice were protected from liver inflammation in a malaria infection model (Knackstedt et al., 2019). However, NETs play a protective role in bacterial sepsis, in which DNASE1 administration was shown to impair NETosis and control infection (Meng et al., 2012). We did not observe increased NETosis or NET-driven coagulation in DNase-deficient mice during *S. aureus* infection, despite extensive neutrophilia. Moreover, we did not observe the reported NET-induced pathology in DNASE1/DNASE1L3-deficient mice during LPS/*E. coli*–induced sepsis (Jiménez-Alcázar et al., 2017). Whereas this may have been caused by different reagents such as the *E. coli* strain, our treatment regimen produced the intended effect, i.e., massive neutrophilia along with other systemic changes. On the other hand, the discrepancy may in part reflect different phenotype readouts; in particular, Jiménez-Alcázar et al. used a poorly defined "distress" as the sole criterion for non-survival, whereas we used an objective primary criterion of weight loss. Overall, our data do not support the role of secreted DNases in NET processing during systemic *S. aureus* infection and suggest their NET-independent role in innate infection control.

Our results suggest that DNases help control *S. aureus* infection through their ability to digest bacterial biofilms. *S. aureus*, like many other bacterial species, relies on eDNA-rich biofilms to evade host immune responses (Bhattacharya et al., 2018), establish active infection, and increase resistance to antibiotics (Paharik and Horswill, 2016). *S. aureus* biofilms have previously been associated with multiple diseases such as osteomyelitis (Brady et al., 2006), endocarditis (Xiong et al., 2005), and implant-associated infections (Cassat et al., 2007; Gries et al., 2020; Heim et al., 2020). Consistent with the well-established pathogenesis of bloodborne *S. aureus* infection (Cheng et al., 2011; Kim et al., 2014; Thomer et al., 2016), kidneys represented the major site of infection in our studies as evidenced by high bacterial burdens and organ pathology. Using 5-mC detection as a novel approach to differentiate between host and bacterial eDNA, we found that DNASE1/DNASE1L3 double-deficient mice formed larger biofilm structures containing bacterial eDNA in the kidneys. The formation of biofilm in the kidneys was further supported by staining with anti-WTA antibody and by the inability of antibiotic treatment to rescue the survival in DNase-deficient animals. Although no single method can detect biofilm formation in tissues with complete specificity, the combination of these approaches documents increased biofilm formation in the kidneys of DNase-deficient mice. Taken together with elevated bacterial burdens, tissue pathology, and impairment of kidney function, these results suggest defective biofilm control as the likely basis of increased susceptibility of these mice to infection.

The ability of DNASE1 and its homolog DNASE1L2 to disperse bacterial biofilms in vitro has been demonstrated previously (Conover et al., 2011; Eckhart et al., 2007; Sharma and Pagedar Singh, 2018). However, the role of these and other mammalian DNases in biofilm formation during bacterial infection in vivo has not been examined by genetic approaches. Our data demonstrate the requirement for (rather than the mere ability of) extracellular DNases for biofilm dispersal and reveal the unexpected synergy between DNASE1 and a newly implicated homologous DNase, DNASE1L3. Notably, the deletion of the staphylococcal nuclease (Nuc1) did not rescue the phenotype of DNASE1/DNASE1L3 double-deficient mice (data not shown). This is consistent with the complex regulation and role of Nuc1 in biofilm formation (Forson et al., 2020; Kiedrowski et al., 2011; Mann et al., 2009) and highlights the dominant role of host DNases in the process. Furthermore, bacterial lesions in DNase-deficient mice showed the disruption of the quintessential *S. aureus* kidney abscess structure, which is composed of a bacterial community surrounded by pseudocapsule of fibrin deposits and a large infiltration of neutrophils and macrophages (Cheng et al., 2011; Cheng et al., 2009; Thammavongsa et al., 2013). The reduction of neutrophil infiltration suggests that the expanded biofilm shields bacteria from the immune system, whereas DNases disrupt the biofilm and thereby facilitate abscess formation and containment of the infection.

The ability of secreted DNases to digest biofilms prompted us to test the therapeutic utility of systemic DNase administration

during *S. aureus* bloodstream infection. To this end, we chose Dornase alfa (Pulmozyme), a recombinant human DNASE1 used for the treatment of cystic fibrosis (Wagener and Kupfer, 2012; Yang and Montgomery, 2021). Dornase is applied via a nebulizer to the lungs of patients with cystic fibrosis and reduces the viscosity of their sputum by digesting DNA. Previous attempts to deliver recombinant DNASE1 systemically were not effective in diseases such as SLE (Davis et al., 1999), while its antimicrobial activity was tested only in a local infection model (Conover et al., 2011). We found that systemic delivery of Dornase was able to reduce biofilm formation in the kidneys of *S. aureus*–infected mice and enhance their survival. It is likely that systemic delivery of recombinant DNase does not fully recapitulate the natural distribution of extracellular DNases that are expressed in a cell type–specific manner and thus are likely to form local gradients. Specifically, DNASE1 is expressed in the kidney parenchyma while DNASE1L3 is expressed in myeloid cells infiltrating tissues, likely creating high local concentrations of DNase activity within the kidney. Future attempts at therapy using DNases may be improved by targeted delivery, i.e., via cell therapy or tissue-specific viral vectors. Another major challenge would be to improve the stability of native DNASE1 and/or DNASE1L3, which are relatively small proteins that are expected to have a short half-life. With these improvements pending, our results provide proof of principle for the application of secreted DNases in antimicrobial therapy, specifically to mitigate tissue damage by biofilm-forming bacteria such as *S. aureus*.

In closing, our study establishes an innate defense role for mammalian secreted DNases DNASE1 and DNASE1L3 in the removal of *S. aureus* biofilms; this may reflect the prevention of biofilm formation, digestion of existing biofilms, or both processes. By doing so, these DNases facilitate the infiltration of bacterial lesions by granulocytes and their containment in an abscess. We also demonstrate the potential therapeutic value of DNase administration during systemic infection with *S. aureus*. The formation of biofilms and the use of eDNA for this process is a conserved virulence strategy employed by multiple microbes, including bacterial and fungal pathogens. Thus, DNASE1L3 and DNASE1 likely have a broader function in innate immunity, beyond *S. aureus*, through their containment of microbes that exploit eDNA-mediated biofilms for their pathophysiology; this notion could be explored further using different microbial pathogens and vertebrate hosts. Altogether, our data help elucidate the ancestral function of DNases in innate immunity and warrant the repurposing and/or development of recombinant DNases to combat infections with biofilm-forming pathogens.

Materials and methods

Mice

All animal studies were performed according to the investigators' protocol approved by the Institutional Animal Care and Use Committees of the New York University School of Medicine. The *Dnase1l3*-deficient mouse strain (*Dnase1l3*^{tm1Tac}) was originally obtained from Taconic Inc. and backcrossed to C57BL/6 background as described previously (Sisirak et al., 2016). Mice carrying a targeted allele of *Dnase1* (*Dnase1*$^{tm1.1(KOMP)Vlcg}$) on a C57BL/6 background were obtained from the Knockout Mouse Project and crossed with WT C57BL/6 or *Dnase1l3*-deficient mice to obtain *Dnase1*-deficient and *Dnase1*/*Dnase1l3* double-deficient mice, respectively. WT control mice of C57BL/6 background were bred in the same animal facility or purchased from Taconic, Inc. and maintained in the same facility. All mice were age- and sex-matched when comparing groups unless otherwise specified.

S. aureus infection

S. aureus strain USA300 LAC clone AH1263 (Boles et al., 2010) was used for in vivo infection studies. The bacteria were subcultured in tryptic soy broth (TSB) at 1:100 for 3 h at 37°C with shaking. Bacteria were centrifuged at 4,000 rpm for 5 min and washed two times with 1× PBS. The bacteria were normalized OD to ∼10^9 CFU/ml and diluted to the indicated inoculum in PBS for infection. Mice (8–10 wk-old) were anesthetized with Avertin (2,2,2-tribromoethanol dissolved in tert-Amyl alcohol and diluted to a final concentration of 2.5% vol/vol in 0.9% sterile saline) by i.p. injection. For survival experiments, mice were infected i.v. at 1 × 10^7 CFU by retro-orbital injection. Signs of morbidity (weight loss, ruffled fur, hunched posture, paralysis, inability to walk, or inability to consume food or water) were monitored for 8 d after infection. Unless indicated otherwise, mice that lost >20% of initial weight (primary criterion) and showed other above-mentioned symptoms (secondary criteria) were designated as non-surviving and euthanized. For analysis, mice were sacrificed at 18 or 72 h after infection. To determine bacterial burden, the liver, kidneys, spleen, lungs, and heart were removed, homogenized in sterile PBS, serially diluted, and plated on tryptic soy agar, and CFU counts were enumerated.

Induction of sterile inflammation using LPS and *E. coli*

Treatment was performed as described by Jiménez-Alcázar et al. (2017). Mice were treated with three daily intraperitoneal injections of 1 µg/g of LPS from *Salmonella enterica* serotype typhimurium (L6511; Sigma-Aldrich) diluted in sterile PBS. With the last dose, mice received an i.v. injection of 1.5 × 10^7 heat-killed *E. coli*/gm body weight. The shown survival time indicates the time after *E. coli* injection. Mice that reached 20% weight loss prior to *E. coli* injection were excluded from the survival analysis. Blood and organs were collected at the time of euthanasia. Mice were scored as "non-surviving" if the animals showed rare signs of severe distress (hunched posture, paralysis, inability to walk, irresponsiveness to touch, or inability to consume food or water) or if they reached 20% weight loss. All surviving mice were euthanized and scored as "surviving" 42 h after the i.v. injection of heat-killed *E. coli*. *E. coli* (ATCC25922) was grown overnight at 37°C with shaking in lysogeny broth media. Bacteria were pelleted by centrifuging at 4,000 *g* for 5 min, washed with PBS, and resuspended in PBS. Aliquots of 1.5 × 10^9 bacteria/ml were incubated at 70°C for 15 min to heat-kill the bacteria. Aliquots were stored at −20°C until further use.

Dornase treatment

Mice were infected with *S. aureus* as described above and treated with Pulmozyme (Genentech, Inc.) or buffer only (containing

calcium chloride dihydrate 0.15 mg/ml and sodium chloride 8.77 mg/ml) by i.v. tail vein injection at 4, 24, 48, 72, and 96 h after infection. Signs of morbidity were monitored for 7 d after infection; mice that lost >30% of initial weight and showed other morbidity symptoms were designated as non-surviving and euthanized. Bacterial burden was determined as described above.

Vancomycin treatment

Mice were infected with *S. aureus* as described above and treated with Vancomycin (20 mg/kg in 0.1 ml PBS) or PBS only by a single s.c. injection in the groin area at 24 h after infection. Signs of morbidity were monitored for 7 d after infection; mice that lost >30% of initial weight and showed other morbidity symptoms were designated as non-surviving and euthanized.

Preparation of plasma and serum samples

For terminal bleeds, mice were anesthetized by i.p. injection of 100 mg/kg ketamine/10 mg/kg xylazine in sterile PBS. Blood was isolated by cardiac puncture using a 26G syringe and transferred into EDTA-coated tubes (Kent Scientific). For serial bleeding, mice were cheek bled into EDTA-coated tubes (Kent Scientific). Where indicated, complete blood counts (CBC) were analyzed using Element HT5 Hematology Analyzer (Heska Corporation). For plasma isolation, blood was centrifuged at 1,000 *g* for 10 min and the supernatant was centrifuged again at the same speed for 10 min. For serum isolation, blood was collected into Eppendorf tubes, left to coagulate at room temperature for 1 h, and centrifuged at 3,000 *g* for 30 min at room temperature.

Analysis of autoreactivity and immune complex deposition

ELISA and ELISPOT for autoantibodies to nucleosomes and dsDNA (both from calf thymus) were performed exactly as described (Soni et al., 2020).

Measurement of plasma cytokines in mice

Cytokine concentrations in plasma were assessed using the 13-plex LEGENDplex Mouse Inflammation Panel (BioLegend) following the protocol provided. Data were acquired using Attune NxT (Thermo Fisher Scientific) flow cytometer and analyzed using the LEGENDplex data analysis software (BioLegend).

Detection of NETs in plasma

Nunc MaxiSorp plates were coated with 50 µl/well of 4 µg/ml anti-MPO antibody (R&D Systems) in PBS overnight at 4°C. Plates were washed three to five times with PBS/0.05% Tween and blocked with PBS/1% BSA for 1.5 h at room temperature. Plates were washed and 50 µl of undiluted plasma samples were added to each well and incubated overnight at 4°C. Plates were washed three to five times with PBS/0.05% Tween, and 50 µl of mouse anti-dsDNA (1:2,000; Abcam) diluted in 1× PBS/1% BSA was added and incubated overnight at 4°C. Plates were washed and alkaline phosphatase–conjugated anti-mouse IgG Fcγ2a (1:5,000; Jackson Immunoresearch) diluted in PBS/1% BSA was added and incubated for 3 h at 4°C, followed by development with diethanolamine substrate buffer (Thermo Fisher Scientific) and p-nitrophenyl phosphate substrate tablets (Sigma-Aldrich). Undiluted bronchoalveolar lavage fluid from mice with lung neutrophilia (Fogli et al., 2013) was used as a positive control on the same plate.

Flow cytometry of murine splenocytes and peripheral blood cells

Cell suspensions of peripheral blood or splenocytes were subjected to red blood cell lysis, washed, and resuspended in staining buffer (1% FCS + 2% BSA + 1 mM EDTA in PBS). Cells were Fc-blocked with TruStain FcX (BioLegend) for 10–15 min at 4°C and stained with indicated cell surface markers for 20 min at 4°C. Samples were acquired using Attune NxT (Thermo Fisher Scientific) flow cytometer and analyzed using FlowJo software version 9 or 10 (Tree Star). Antibodies and dilutions were as follows: CD8α-FITC (1:800; clone 53-6.7; ebioscience), CD8α-APC-Cy7 (1:800; clone 53-6.7; ebioscience), CD8α-PE-Cy7 (1:800; clone 53-6.7; ebioscience), CD8α-BV510 (1:400; clone 53-6.7; BD), CD4-BV711 (1:800–1:1,000; clone RM4-5; BioLegend), TCRβ-PacBlue (1:300; clone H57-597; Invitrogen), TCRβ-BV510 (1:200; clone H57-597; BioLegend), B220-PE-Cy7 (1:300; clone RA3-6B2; ebioscience), B220-BV605 (1:300; clone RA3-6B2; BioLegend), CD11c-APC-Cy7 (1:150; clone N418; Invitrogen), CD11c-PE (1:400; clone N418; ebioscience), CD11b-APC-Cy7 (1:400; clone M1/70; Invitrogen), CD11b-APC (1:200; clone M1/70; Invitrogen), CD11b-PE (1:800; clone M1/70; ebioscience), Ly6G-PacBlue (1:800; clone 1A8; BioLegend), Ly6G-PE-Cy7 (1:800; clone 1A8; BioLegend), Ly6c-APC (1:800; clone HK1.4; Invitrogen), Ly6c-PE-Dazzle (1:800; clone HK1.4; BioLegend), Sca1-Percp-Cy5.5 (1:200; clone D7; Invitrogen), ICAM-1/CD54-APC (1:200; clone 3E2; BD), ICAM-1/CD54-FITC (1:200; clone 3E2; BD), and Live Dead stain (1:1,000; cat# L34965; Thermo Fisher Scientific).

Flow cytometry of murine kidney immune populations

After dissection, kidney capsules were removed and kidneys were minced in 4 ml of digestion media composed of 20% FCS, 1 mM $MgCl_2$, 1 mM $CaCl_2$, 1% Glutamine (Thermo Fisher Scientific), 1 mg/ml collagenase D (Roche), and 0.1 mg/ml DNASE1 (Millipore) in RPMI medium 1640 with *L*-glutamine (Thermo Fisher Scientific). The minced organs were then incubated at 37°C for 45 min with rigorous shaking. The digestion was stopped using 10 ml of stop solution composed of 20% FCS + 1 mM EDTA in RPMI medium 1640 with *L*-glutamine (Thermo Fisher Scientific). The samples were inverted and gently pressed through a 70-µm cell strainer. The cell suspension was centrifuged at 400 *g* for 10 min at 4°C and the pellet was resuspended in 4 ml of 40% Percoll (Sigma-Aldrich) diluted in sterile 1× PBS. The cells were then added to a 15 ml conical tube and a glass Pasteur pipet was used to slowly deliver 4 ml of an 80% Percoll solution to the bottom of the tube. The cells were then centrifuged at 1,500 *g* for 30 min at room temperature without acceleration or breaks. The lymphocyte layer was then aspirated into a new tube with fresh 10% FCS in RPMI medium 1640 with *L*-glutamine. The cells were centrifuged one last time at 400 *g* for 10 min at 4°C and resuspended in staining buffer (1% FCS + 2% BSA + 1 mM EDTA in 1× PBS). Cells were Fc blocked using TruStain FcX (BioLegend) for 10–15 min at 4°C and stained with

indicated cell surface markers for 20 min at 4°C. Samples were acquired using Attune NxT (Thermo Fisher Scientific) flow cytometer and analyzed using FlowJo software version 9 or 10 (Tree Star). Antibodies and dilutions were as follows: CD8α-AF700 (1:400; clone 53-6.7; Invitrogen), CD4-APC (1:400; clone GK1.5; ebioscience), CD4-PE-Cy7 (1:400; clone RM4-5; ebioscience), CD45-Percp-Cy5.5 (1:200; clone 30-F11; BD), TCRβ-PacBlue (1:200; clone H57-597; Invitrogen), TCRβ-BV605 (1:400; clone H57-597; BD), B220-BV711 (1:400; clone RA3-6B2; BD), B220-BV605 (1:400; clone RA3-6B2; BioLegend), CD11c-PE (1:200; clone N418; ebioscience), F4/80-FITC (1:100; clone BM8; Invitrogen), CD11b-APC-Cy7 (1:200; clone M1/70; Invitrogen), Ly6G-PE-Cy7 (1:400; clone 1A8; BioLegend), Ly6c-APC (1:400; clone HK1.4; Invitrogen), Ly6c-PE-Dazzle (1:600; clone HK1.4; BioLegend), and Live Dead stain (1:1,000; cat# L34965; Thermo Fisher Scientific).

Histological analysis of mouse organs

For the analysis of SLE-induced kidney pathology, we used at least four to five female mice per genotype. Females were chosen in this case because they showed a more severe pathology in previously characterized *Dnase1*-deficient mice (Kenny et al., 2019). One half of each kidney was fixed in 10% neutral formalin for 24 h at room temperature, stored in 70% ethanol, and subsequently embedded in paraffin. For the analysis of *S. aureus*–induced organ pathology, we used at least four mice per group at the 18-h time point for all organs, at least four mice per group at the 72-h time point for the lung, liver, and heart (WT and $D1^{-/-}D1L3^{-/-}$), and at least 12 mice per group at the 72-h time point for the kidney. One half of each kidney, the left lung, and a section of the liver were fixed and embedded as above. For the analysis of lungs following sterile inflammation, we used at least seven mice per group. Each of the lobes of the lung was separated and fixed as above.

Sections (5 mm) were stained with H&E and captured using the PerkinElmer Vectra multispectral imaging system at 40× magnification (Leica Biosystems digital image hub). Sections were evaluated by a board-certified pathologist (A. Moreira) who was blinded to the sample identity. For the analysis of kidney damage in *S. aureus* infection, scores between 0 and 3 were assigned based on a combination of immune infiltration, tissue necrosis, and the fraction of normal tissue remaining. Sections from at least 12 mice per group were evaluated simultaneously. For the analysis of glomeruli in DNase-deficient mice, the Halo AI module of Halo software (Indica Labs) was used. The Halo AI DenseNet module was trained to develop a tissue classification system using kidney sections to identify glomeruli and measure the size. The AI-generated data were manually checked to delete any suboptimally classified glomeruli.

For Gram staining, deparaffinized sections were rehydrated, rinsed, stained with Crystal Violet (Poly Scientific R&D) for 2 min, rinsed, and stained with Gram's iodine (EM Sciences) for 2 min (all rinses in distilled water). Sections were rinsed to remove excess iodine, blotted one slide at a time with a slightly damp filter paper, quickly dipped in acetone for complete decolorization, and rinsed. Sections were then stained in basic fuchsin (Poly Scientific R&D) for 5 min, rinsed, differentiated with Gallego's solution (Poly Scientific R&D) for 5 min, rinsed, blotted, and successively dipped thrice in acetone, picric acid-acetone (Poly Scientific R&D), and acetone, and then five times in acetone–xylene mixture (1:2). Finally, sections were cleaned in xylene for 1 min two to four times and mounted with permount (Thermo Fisher Scientific). Using this protocol, Gram-positive bacteria were blue, gram-negative bacteria were red, and background tissue was yellow.

EM

Mice were infected with *S. aureus* as described above and sacrificed 72 h after infection. Kidneys were harvested and immediately fixed in freshly made 4% paraformaldehyde (PFA) in 0.1 M phosphate buffer (PB, pH 7.2) at room temperature for 1 h with rotation. The kidney was then cut in half longitudinally and continued to fix in 4% PFA in PB overnight at 4°C. Bacterial lesion areas were identified under a dissecting microscope.

For scanning EM (SEM), 1-mm-thick kidney slices were cut after initial fixation and fixed in 2.5% glutaraldehyde in PB overnight at 4°C. They were then rinsed 3× in 0.1 M PB (pH 7.2) for 10 min, postfixed with 1% osmium tetroxide aqueous solution for 1 h, dehydrated in 30, 50, 70, 85, and 95% alcohol (15 min each time) and then washed in 100% ethanol 3×, 15 min each at room temperature. Samples were critically dried using Tousimis Autosamdri 931, glued on SEM stab, and sputter-coated with 80% Pt/20% Pd to 8 nm by DESK V TSC HP Denton Vacuum. Images were acquired on a Zeiss Gemini300 FESEM using SE2 detector at 4 kv with 15.3 mm working distance. For serial block-face scanning EM and transmission EM, 1 × 1 × 1 mm pieces of kidney tissue were dissected from the initially fixed tissue and fixed in freshly made fixative in 0.1 M cacodylate buffer (CB; pH 7.2) containing 4% PFA, 2.5% glutaraldehyde at 4°C for 2–3 d. They were then washed with 0.1 M CB 3×, 10 min each and added to reduced 2% osmium tetroxide/1.5% potassium ferrocyanide in CB for 1.5 h at room temperature in the dark. They were then washed, stained in 1% TCH solution (0.1 g thiocarbohydrazide in 10 ml water filtered through 0.22-µm Millipore syringe) for 20 min, washed, transferred to 2% osmium tetroxide in ddH_2O for 40 min at room temperature, washed, and incubated in 1% uranyl acetate in water overnight at 4°C in the dark (all washes 5× for 3 min with double-distilled water at room temperature). The following day, the samples were washed, stained en bloc with Walton's lead aspartate staining solution at 60°C for 30 min, washed and dehydrated in 30, 50, 70, 85, 95 and 100% ethanol, 15 min each, and in propylene oxide 2×, 10 min each. Samples were then infiltrated in 100% PO:Spurr 1:1 solution for 4 h at room temperature, 100% Spurr overnight at room temperature, and 100% fresh Spurr for 2 h at room temperature the following day. Samples were finally embedded and polymerized at 60°C for 48 h and then 100°C for 2 h.

For transmission EM, the sample block was trimmed, and 70-nm thin sections were collected on slot grids and imaged under Talos120C TEM (Thermo Fisher Scientific) with Gatan OneView camera. For serial block face scanning EM, the sample block was mounted on an aluminum specimen pin (Gatan) using silver conductive epoxy (Ted Pella, Inc.) to electrically ground the tissue block. The specimen was trimmed again and sputter-

coated with 4 nm of gold-palladium $Au_{80}Pd_{20}$ (Denton Vacuum DESKV sputter coater, Denton Vacuum). Serial block face imaging was performed using a Gatan OnPoint BSE detector in a Zeiss Gemini300 VP FESEM equipped with a Gatan 3View automatic microtome unit. The system was set to cut sections with 100 nm thickness, imaged with Focus Charge Compensation gas injection set at 15% to reduce sample charge. Images of the block face were recorded after each round of sectioning with beam acceleration set at 1.2 keV with a beam dwell time of 1.0 µs/pixel. Each frame was 90 × 90 µm with a pixel size of 6 nm. Automated data acquisition was managed using Gatan Digital Micrograph (version 3.31) software. A stack of 480 slices was collected from the tissue block resulting in a final collection volume of 90 × 90 × 48 µm. The stack was aligned and assembled using ImageJ; segmentation and movies were generated using Dragonfly 4.1 (Object Research Systems).

Detection of bacteria and biofilms by immunohistochemistry and immunocytochemistry

One half of each kidney was fixed with periodate–lysine–PFA buffer overnight at 4°C, dehydrated for 8–10 h in 30% sucrose, and frozen in OCT (Fisher Healthcare). For *S. aureus*, Ly-6G, and WTA staining, 5-µm-thick kidney sections were blocked with 2% BSA in Tris-buffered saline (TBS) and incubated with rabbit anti–*S. aureus* (1:400; ab20902; Abcam), rat anti-Ly6G (1:800; clone 1A8; InvivoPlus), and human IgG3-anti-WTA antibody (de Vor et al., 2022; 1:130) overnight at 4°C. The sections were washed three times with 1% BSA in TBS and incubated with goat anti-rabbit IgG-AF488 (1:500; Invitrogen), mouse anti-rat IgG2a-AF647 (1:1,000; clone 2A 8F4; Abcam), goat anti-human IgG3-AF647 (1:300; SouthernBiotech), and with DAPI for 1 h at 4°C. For 5-mC staining, 5-µm-thick kidney sections were first permeabilized with 1.5 M hydrogen chloride (Fisher Chemical). The sections were washed two times with PBS, blocked with 2% BSA in TBS, and incubated with rabbit anti–5-mC antibody (1:80; clone D3S2Z; Cell Signaling) overnight at 4°C. The sections were washed three times with 1% BSA in TBS and incubated with goat anti-rabbit IgG-AF488 (1:500; Invitrogen) and DAPI for 1 h at 4°C. The sections were again washed three times with 1% BSA in TBS and then mounted with cover glass over tissue sections using ProLong Diamond Antifade Mountant (Invitrogen). For immunocytochemistry, HEK 293 cells were cultured in 6-well plates and stained using the same technique as above. All antibodies were diluted in blocking solution. Images were taken using a Keyence BZ-X710 fluorescence microscope at 20× magnification. Immunofluorescence intensities were quantified using ImageJ 1.53 k image processing and analysis software (National Institutes of Health [NIH]); color intensity of images was subsequently enhanced using Affinity Designer (Serif) consistently on entire images of control and test sections.

For the quantification of biofilm, anti–*S. aureus* and DAPI staining were used to identify the bacterial lesions and the surrounding DAPI-positive regions. These regions were then gated on a serial section stained with anti–5-mC and DAPI. The thresholds of 5-mC and DAPI fluorescence intensity were determined based on the staining of kidneys from uninfected WT mice using ImageJ 1.53 k software (NIH). The areas above the 5-mC and DAPI fluorescence intensity thresholds were defined within the gated regions and the former was subtracted from the latter to yield the area of DAPI-positive, 5-mC–negative biofilm. At least eight mice per genotype were used for the analysis.

DNASE1L3 protein purification

This was done as described (Hartl et al., 2021). Briefly, 293T cells expressing FLAG-tagged human DNASE1L3 were cultured and the supernatants were incubated with magnetic anti-FLAG M2 beads (Sigma-Aldrich) overnight at 4°C. The beads were incubated with 0.25 mg/ml of FLAG peptide and the eluted protein was quantified by SDS-PAGE with BSA as a standard.

In vitro biofilm dispersal

96-well flat bottom plates were coated with 100 µl of 20% human plasma (P9523; Sigma-Aldrich) diluted in carbonate–bicarbonate buffer (0.05 M, pH 9.6) at 4°C overnight. *S. aureus* was cultured overnight in 5 ml TSB supplemented with 0.5% dextrose and 3% NaCl. The overnight culture was diluted 1:200 in TSB supplemented with 0.5% dextrose and 3% NaCl and 200 µl was added to each well of the 96-well plate. The biofilms were allowed to grow undisturbed for 24 h at 37°C. Recombinant human DNASE1L3 (purified as described above) and DNASE1 (Abcam) were prediluted in dilution media containing 0.1 mg/ml BSA (NEB) in HBSS without calcium, magnesium, or Phenol Red (Thermo Fisher Scientific) and then added to the digestion media (2 mM $CaCl_2$ + 2 mM $MnCl_2$ in HBSS) at a range of concentrations. The media was then removed and 100 µl of digestion media containing recombinant enzymes was then added to each well and incubated for 1 h at 37°C. The wells were washed gently 3× with PBS, rocking for ∼5 min between each wash. Any remaining biofilm was then fixed with 200 µl 95% ethanol in each well. After drying for 20 min, the samples were stained with 100 µl 0.1% crystal violet (Thermo Fisher Scientific) for 10 min. The plate was then washed 4× with 200 µl PBS, rocking for ∼5 min between each wash. To elute the crystal violet, 200 µl of 33% acetic acid was added to each well and incubated for 10 min at room temperature with rocking. Elutions were diluted in PBS as needed and OD at 595 nm was recorded.

Statistical analysis

Statistical analyses were performed using the Prism software version 9 (GraphPad). Normal distribution of data was not assumed unless otherwise specified. Statistical significance between two unpaired experimental groups was determined by the non-parametric Mann–Whitney test (also referred to as Wilcoxon rank–sum test), unless otherwise specified. For paired groups, normality was assessed using the Shapiro–Wilk test. If the data were normally distributed, a parametric paired *t* test was used. If the data were not normally distributed, a non-parametric Wilcoxon matched-pairs signed rank test was used. The non-parametric Kruskal–Wallis test followed by the Dunn's multiple-comparison test was used for statistical analysis of more than two groups receiving the same treatment. Two-way ANOVA followed by Tukey's multiple-comparison test was used for statistical analysis of more than two groups receiving different treatments (e.g., *S. aureus* vs. LPS/*E. coli*). For survival

curves, statistical significance between the two groups was determined by log-rank (Mantel–Cox) test and P values were adjusted for multiple comparisons using Bonferroni correction. All P values were two-tailed and differences were considered significant for P values < 0.05 (*), <0.01 (**), <0.001 (***), and <0.0001 (****).

Online supplemental material

Fig. S1 shows histopathology of multiple organs after systemic infection with *S. aureus*. Fig. S2 shows Gram staining of kidneys from *S. aureus*–infected D1$^{-/-}$D1L3$^{-/-}$ mice. Fig. S3 shows the analysis of blood cells after the infection with *S. aureus* or the induction of sterile inflammation with LPS. Fig. S4 shows the analysis of the kidneys from *S. aureus*–infected D1$^{-/-}$D1L3$^{-/-}$ mice by transmission EM. Fig. S5 shows immunofluorescent analysis of kidney sections from WT or D1$^{-/-}$D1L3$^{-/-}$ mice 48 h after infection with *S. aureus*. Video 1 shows serial block-face scanning EM analysis of a bacterial lesion in the kidney of a *S. aureus*–infected D1$^{-/-}$D1L3$^{-/-}$ mouse.

Data availability

All data underlying the research are presented in the published article and its online supplemental material and/or available from the corresponding authors upon reasonable request.

Acknowledgments

We thank Suzane Rooijakkers (UMC Utrecht, Utrecht, Netherlands) for kindly providing the anti-WTA mAb, Sergei Koralov (New York University, New York, NY, USA) for the NET-containing control sample, and Alice Liang, Joseph Sall, Chris Petzold, and Kristen Dancel-Manning of the NYU Langone Health Division of Advanced Research Technologies Microscopy Lab for assistance with EM. Microscopy shared resource is supported by NIH grant CA016087 at the Laura and Isaac Perlmutter Cancer Center. The Gemini300 SEM with 3View was purchased with the support of NIH grant OD019974. The nuc mutant of *S. aureus* was obtained from the Nebraska transposon mutant library (Network of Antimicrobial Resistance in *S. aureus* program), which was supported under the NIH-National Institute of Allergy and Infectious Diseases contract HHSN272200700055C.

This study was supported by the NIH grants AR071703 and AR070591 (B. Reizis), AI100853 (L. Serpas, A. Rashidfarrokhi); AR069515 and GM136573 (L. Serpas); AI137336, AI099394, AI105129; and AI121244 (V.J. Torres). It was also supported by the Lupus Research Alliance and the Colton Center for Autoimmunity (B. Reizis), the Uehara Memorial Foundation (S. Makita), and the Cystic Fibrosis Foundation (K.A. Lacey). V.J. Torres is a Burroughs Wellcome Fund Investigator in the pathogenesis of infectious diseases.

Author contributions: K.A. Lacey, L. Serpas, S. Makita, Y. Wang, A. Rashidfarrokhi, C. Soni, S. Gonzalez performed experiments and analyzed results. A. Moreira analyzed results. V.J. Torres and B. Reizis supervised the project and analyzed results. K.A. Lacey, L. Serpas, S. Makita, V.J. Torres, and B. Reizis wrote the manuscript.

Disclosures: V.J. Torres reported grants from Jassen Biotech, Inc. and personal fees from Jassen Biotech, Inc. outside the submitted work. B. Reizis is an advisor for Related Sciences and a co-founder of Danger Bio, companies developing therapeutics for autoimmune diseases. No other disclosures were reported.

Submitted: 23 June 2022
Revised: 18 January 2023
Accepted: 1 March 2023

References

Al-Mayouf, S.M., A. Sunker, R. Abdwani, S.A. Abrawi, F. Almurshedi, N. Alhashmi, A. Al Sonbul, W. Sewairi, A. Qari, E. Abdallah, et al. 2011. Loss-of-function variant in DNASE1L3 causes a familial form of systemic lupus erythematosus. *Nat. Genet.* 43:1186–1188. https://doi.org/10.1038/ng.975

Barrat, F.J., K.B. Elkon, and K.A. Fitzgerald. 2016. Importance of nucleic acid recognition in inflammation and autoimmunity. *Annu. Rev. Med.* 67: 323–336. https://doi.org/10.1146/annurev-med-052814-023338

Basit, A., J. Reutershan, M.A. Morris, M. Solga, C.E. Rose Jr, and K. Ley. 2006. ICAM-1 and LFA-1 play critical roles in LPS-induced neutrophil recruitment into the alveolar space. *Am. J. Physiol. Lung Cell. Mol. Physiol.* 291:L200–L207. https://doi.org/10.1152/ajplung.00346.2005

Belot, A., G.I. Rice, S.O. Omarjee, Q. Rouchon, E.M.D. Smith, M. Moreews, M. Tusseau, C. Frachette, R. Bournhonesque, N. Thielens, et al. 2020. Contribution of rare and predicted pathogenic gene variants to childhood-onset lupus: A large, genetic panel analysis of British and French cohorts. *Lancet Rheumatol.* 2:e99–e109. https://doi.org/10.1016/S2665-9913(19)30142-0

Bhattacharya, M., E.T.M. Berends, R. Chan, E. Schwab, S. Roy, C.K. Sen, V.J. Torres, and D.J. Wozniak. 2018. *Staphylococcus aureus* biofilms release leukocidins to elicit extracellular trap formation and evade neutrophil-mediated killing. *Proc. Natl. Acad. Sci. USA.* 115:7416–7421. https://doi.org/10.1073/pnas.1721949115

Boles, B.R., M. Thoendel, A.J. Roth, and A.R. Horswill. 2010. Identification of genes involved in polysaccharide-independent *Staphylococcus aureus* biofilm formation. *PLoS One.* 5:e10146. https://doi.org/10.1371/journal.pone.0010146

Brady, R.A., J.G. Leid, A.K. Camper, J.W. Costerton, and M.E. Shirtliff. 2006. Identification of *Staphylococcus aureus* proteins recognized by the antibody-mediated immune response to a biofilm infection. *Infect. Immun.* 74:3415–3426. https://doi.org/10.1128/IAI.00392-06

Brinkmann, V., U. Reichard, C. Goosmann, B. Fauler, Y. Uhlemann, D.S. Weiss, Y. Weinrauch, and A. Zychlinsky. 2004. Neutrophil extracellular traps kill bacteria. *Science.* 303:1532–1535. https://doi.org/10.1126/science.1092385

Bygrave, A.E., K.L. Rose, J. Cortes-Hernandez, J. Warren, R.J. Rigby, H.T. Cook, M.J. Walport, T.J. Vyse, and M. Botto. 2004. Spontaneous autoimmunity in 129 and C57BL/6 mice-implications for autoimmunity described in gene-targeted mice. *PLoS Biol.* 2:E243. https://doi.org/10.1371/journal.pbio.0020243

Cassat, J.E., C.Y. Lee, and M.S. Smeltzer. 2007. Investigation of biofilm formation in clinical isolates of *Staphylococcus aureus*. *Methods Mol. Biol.* 391:127–144. https://doi.org/10.1007/978-1-59745-468-1_10

Chan, M.P., M. Onji, R. Fukui, K. Kawane, T. Shibata, S. Saitoh, U. Ohto, T. Shimizu, G.N. Barber, and K. Miyake. 2015. DNase II-dependent DNA digestion is required for DNA sensing by TLR9. *Nat. Commun.* 6:5853. https://doi.org/10.1038/ncomms6853

Cheng, A.G., A.C. DeDent, O. Schneewind, and D. Missiakas. 2011. A play in four acts: *Staphylococcus aureus* abscess formation. *Trends Microbiol.* 19: 225–232. https://doi.org/10.1016/j.tim.2011.01.007

Cheng, A.G., H.K. Kim, M.L. Burts, T. Krausz, O. Schneewind, and D.M. Missiakas. 2009. Genetic requirements for *Staphylococcus aureus* abscess formation and persistence in host tissues. *FASEB J.* 23:3393–3404. https://doi.org/10.1096/fj.09-135467

Conover, M.S., M. Mishra, and R. Deora. 2011. Extracellular DNA is essential for maintaining Bordetella biofilm integrity on abiotic surfaces and in the upper respiratory tract of mice. *PLoS One*. 6:e16861. https://doi.org/10.1371/journal.pone.0016861

Crow, Y.J., and N. Manel. 2015. Aicardi-Goutières syndrome and the type I interferonopathies. *Nat. Rev. Immunol.* 15:429–440. https://doi.org/10.1038/nri3850

Crowl, J.T., E.E. Gray, K. Pestal, H.E. Volkman, and D.B. Stetson. 2017. Intracellular nucleic acid detection in autoimmunity. *Annu. Rev. Immunol.* 35:313–336. https://doi.org/10.1146/annurev-immunol-051116-052331

Cue, D., M.G. Lei, and C.Y. Lee. 2012. Genetic regulation of the intercellular adhesion locus in staphylococci. *Front. Cell. Infect. Microbiol.* 2:38. https://doi.org/10.3389/fcimb.2012.00038

Dakheel, K.H., R. Abdul Rahim, V.K. Neela, J.R. Al-Obaidi, T.G. Hun, and K. Yusoff. 2016. Methicillin-resistant *Staphylococcus aureus* biofilms and their influence on bacterial adhesion and cohesion. *BioMed Res. Int.* 2016:4708425. https://doi.org/10.1155/2016/4708425

Davis, J.C., Jr, S. Manzi, C. Yarboro, J. Rairie, I. Mcinnes, D. Averthelyi, D. Sinicropi, V.G. Hale, J. Balow, H. Austin, et al. 1999. Recombinant human Dnase I (rhDNase) in patients with lupus nephritis. *Lupus*. 8:68–76. https://doi.org/10.1191/096120399678847380

de Vor, L., B. van Dijk, K. van Kessel, J.S. Kavanaugh, C. de Haas, P.C. Aerts, M.C. Viveen, E.C. Boel, A.C. Fluit, J.M. Kwiecinski, et al. 2022. Human monoclonal antibodies against *Staphylococcus aureus* surface antigens recognize in vitro and in vivo biofilm. *Elife*. 11:e67301. https://doi.org/10.7554/eLife.67301

Dreiseikelmann, B., and W. Wackernagel. 1981. Absence in Bacillus subtilis and *Staphylococcus aureus* of the sequence-specific deoxyribonucleic acid methylation that is conferred in *Escherichia coli* K-12 by the dam and dcm enzymes. *J. Bacteriol.* 147:259–261. https://doi.org/10.1128/jb.147.1.259-261.1981

Eckhart, L., H. Fischer, K.B. Barken, T. Tolker-Nielsen, and E. Tschachler. 2007. DNase1L2 suppresses biofilm formation by *Pseudomonas aeruginosa* and *Staphylococcus aureus*. *Br. J. Dermatol.* 156:1342–1345. https://doi.org/10.1111/j.1365-2133.2007.07886.x

Fischer, H., S. Szabo, J. Scherz, K. Jaeger, H. Rossiter, M. Buchberger, M. Ghannadan, M. Hermann, H.C. Theussl, D.J. Tobin, et al. 2011. Essential role of the keratinocyte-specific endonuclease DNase1L2 in the removal of nuclear DNA from hair and nails. *J. Invest. Dermatol.* 131:1208–1215. https://doi.org/10.1038/jid.2011.13

Flemming, H.C., J. Wingender, U. Szewzyk, P. Steinberg, S.A. Rice, and S. Kjelleberg. 2016. Biofilms: An emergent form of bacterial life. *Nat. Rev. Microbiol.* 14:563–575. https://doi.org/10.1038/nrmicro.2016.94

Fogli, L.K., M.S. Sundrud, S. Goel, S. Bajwa, K. Jensen, E. Derudder, A. Sun, M. Coffre, C. Uyttenhove, J. Van Snick, et al. 2013. T cell-derived IL-17 mediates epithelial changes in the airway and drives pulmonary neutrophilia. *J. Immunol.* 191:3100–3111. https://doi.org/10.4049/jimmunol.1301360

Forson, A.M., H.C. van der Mei, and J. Sjollema. 2020. Impact of solid surface hydrophobicity and micrococcal nuclease production on *Staphylococcus aureus* Newman biofilms. *Sci. Rep.* 10:12093. https://doi.org/10.1038/s41598-020-69084-x

Foster, T.J., J.A. Geoghegan, V.K. Ganesh, and M. Höök. 2014. Adhesion, invasion and evasion: The many functions of the surface proteins of *Staphylococcus aureus*. *Nat. Rev. Microbiol.* 12:49–62. https://doi.org/10.1038/nrmicro3161

Gries, C.M., T. Biddle, J.L. Bose, T. Kielian, and D.D. Lo. 2020. Staphylococcus aureus fibronectin binding protein A mediates biofilm development and infection. *Infect. Immun.* 88:88. https://doi.org/10.1128/IAI.00859-19

Hakkim, A., B.G. Fürnrohr, K. Amann, B. Laube, U.A. Abed, V. Brinkmann, M. Herrmann, R.E. Voll, and A. Zychlinsky. 2010. Impairment of neutrophil extracellular trap degradation is associated with lupus nephritis. *Proc. Natl. Acad. Sci. USA*. 107:9813–9818. https://doi.org/10.1073/pnas.0909927107

Hartl, J., L. Serpas, Y. Wang, A. Rashidfarrokhi, O.A. Perez, B. Sally, V. Sisirak, C. Soni, A. Khodadadi-Jamayran, A. Tsirigos, et al. 2021. Autoantibody-mediated impairment of DNASE1L3 activity in sporadic systemic lupus erythematosus. *J. Exp. Med.* 218:218. https://doi.org/10.1084/jem.20201138

Heim, C.E., M.E. Bosch, K.J. Yamada, A.L. Aldrich, S.S. Chaudhari, D. Klinkebiel, C.M. Gries, A.A. Alqarzaee, Y. Li, V.C. Thomas, et al. 2020. Lactate production by *Staphylococcus aureus* biofilm inhibits HDAC11 to reprogramme the host immune response during persistent infection. *Nat. Microbiol.* 5:1271–1284. https://doi.org/10.1038/s41564-020-0756-3

Houston, P., S.E. Rowe, C. Pozzi, E.M. Waters, and J.P. O'Gara. 2011. Essential role for the major autolysin in the fibronectin-binding protein-mediated *Staphylococcus aureus* biofilm phenotype. *Infect. Immun.* 79:1153–1165. https://doi.org/10.1128/IAI.00364-10

Jiménez-Alcázar, M., C. Rangaswamy, R. Panda, J. Bitterling, Y.J. Simsek, A.T. Long, R. Bilyy, V. Krenn, C. Renné, T. Renné, et al. 2017. Host DNases prevent vascular occlusion by neutrophil extracellular traps. *Science*. 358:1202–1206. https://doi.org/10.1126/science.aam8897

Kaplan, J.B., K. LoVetri, S.T. Cardona, S. Madhyastha, I. Sadovskaya, S. Jabbouri, and E.A. Izano. 2012. Recombinant human DNase I decreases biofilm and increases antimicrobial susceptibility in staphylococci. *J. Antibiot.* 65:73–77. https://doi.org/10.1038/ja.2011.113

Kenny, E.F., B. Raupach, U. Abu Abed, V. Brinkmann, and A. Zychlinsky. 2019. Dnase1-deficient mice spontaneously develop a systemic lupus erythematosus-like disease. *Eur. J. Immunol.* 49:590–599. https://doi.org/10.1002/eji.201847875

Keyel, P.A. 2017. Dnases in health and disease. *Dev. Biol.* 429:1–11. https://doi.org/10.1016/j.ydbio.2017.06.028

Kiedrowski, M.R., J.S. Kavanaugh, C.L. Malone, J.M. Mootz, J.M. Voyich, M.S. Smeltzer, K.W. Bayles, and A.R. Horswill. 2011. Nuclease modulates biofilm formation in community-associated methicillin-resistant *Staphylococcus aureus*. *PLoS One*. 6:e26714. https://doi.org/10.1371/journal.pone.0026714

Kim, H.K., D. Missiakas, and O. Schneewind. 2014. Mouse models for infectious diseases caused by *Staphylococcus aureus*. *J. Immunol. Methods*. 410:88–99. https://doi.org/10.1016/j.jim.2014.04.007

Knackstedt, S.L., A. Georgiadou, F. Apel, U. Abu-Abed, C.A. Moxon, A.J. Cunnington, B. Raupach, D. Cunningham, J. Langhorne, R. Krüger, et al. 2019. Neutrophil extracellular traps drive inflammatory pathogenesis in malaria. *Sci. Immunol.* 4:4. https://doi.org/10.1126/sciimmunol.aaw0336

Kratofil, R.M., P. Kubes, and J.F. Deniset. 2017. Monocyte conversion during inflammation and injury. *Arterioscler. Thromb. Vasc. Biol.* 37:35–42. https://doi.org/10.1161/ATVBAHA.116.308198

Lee, P.Y., Y. Kumagai, Y. Li, O. Takeuchi, H. Yoshida, J. Weinstein, E.S. Kellner, D. Nacionales, T. Barker, K. Kelly-Scumpia, et al. 2008. TLR7-dependent and FcgammaR-independent production of type I interferon in experimental mouse lupus. *J. Exp. Med.* 205:2995–3006. https://doi.org/10.1084/jem.20080462

Lefrançais, E., B. Mallavia, H. Zhuo, C.S. Calfee, and M.R. Looney. 2018. Maladaptive role of neutrophil extracellular traps in pathogen-induced lung injury. *JCI Insight*. 3:e98178. https://doi.org/10.1172/jci.insight.98178

Lister, J.L., and A.R. Horswill. 2014. Staphylococcus aureus biofilms: Recent developments in biofilm dispersal. *Front. Cell. Infect. Microbiol.* 4:178. https://doi.org/10.3389/fcimb.2014.00178

Mann, E.E., K.C. Rice, B.R. Boles, J.L. Endres, D. Ranjit, L. Chandramohan, L.H. Tsang, M.S. Smeltzer, A.R. Horswill, and K.W. Bayles. 2009. Modulation of eDNA release and degradation affects *Staphylococcus aureus* biofilm maturation. *PLoS One*. 4:e5822. https://doi.org/10.1371/journal.pone.0005822

Mann, P.A., A. Müller, K.A. Wolff, T. Fischmann, H. Wang, P. Reed, Y. Hou, W. Li, C.E. Müller, J. Xiao, et al. 2016. Chemical genetic analysis and functional characterization of staphylococcal wall teichoic acid 2-epimerases reveals unconventional antibiotic drug targets. *PLoS Pathog.* 12:e1005585. https://doi.org/10.1371/journal.ppat.1005585

McCord, J.J., M. Engavale, E. Masoumzadeh, J. Villarreal, B. Mapp, M.P. Latham, P.A. Keyel, and R.B. Sutton. 2022. Structural features of Dnase1L3 responsible for serum antigen clearance. *Commun. Biol.* 5:825. https://doi.org/10.1038/s42003-022-03755-5

Meng, W., A. Paunel-Görgülü, S. Flohé, A. Hoffmann, I. Witte, C. MacKenzie, S.E. Baldus, J. Windolf, and T.T. Lögters. 2012. Depletion of neutrophil extracellular traps in vivo results in hypersusceptibility to polymicrobial sepsis in mice. *Crit. Care*. 16:R137. https://doi.org/10.1186/cc11442

Montanaro, L., A. Poggi, L. Visai, S. Ravaioli, D. Campoccia, P. Speziale, and C.R. Arciola. 2011. Extracellular DNA in biofilms. *Int. J. Artif. Organs*. 34:824–831. https://doi.org/10.5301/ijao.5000051

Mori, G., D. Delfino, P. Pibiri, C. Rivetti, and R. Percudani. 2022. Origin and significance of the human DNase repertoire. *Sci. Rep.* 12:10364. https://doi.org/10.1038/s41598-022-14133-w

Napirei, M., A. Gültekin, T. Kloeckl, T. Möröy, J. Frostegård, and H.G. Mannherz. 2006. Systemic lupus-erythematosus: Deoxyribonuclease 1 in necrotic chromatin disposal. *Int. J. Biochem. Cell Biol.* 38:297–306. https://doi.org/10.1016/j.biocel.2005.10.023

Napirei, M., H. Karsunky, B. Zevnik, H. Stephan, H.G. Mannherz, and T. Möröy. 2000. Features of systemic lupus erythematosus in Dnase1-deficient mice. *Nat. Genet.* 25:177–181. https://doi.org/10.1038/76032

Napirei, M., S. Ludwig, J. Mezrhab, T. Klöckl, and H.G. Mannherz. 2009. Murine serum nucleases--contrasting effects of plasmin and heparin on the activities of DNase1 and DNase1-like 3 (DNase1l3). *FEBS J.* 276: 1059–1073. https://doi.org/10.1111/j.1742-4658.2008.06849.x

Napirei, M., S. Wulf, D. Eulitz, H.G. Mannherz, and T. Kloeckl. 2005. Comparative characterization of rat deoxyribonuclease 1 (Dnase1) and murine deoxyribonuclease 1-like 3 (Dnase1l3). *Biochem. J.* 389:355–364. https://doi.org/10.1042/BJ20042124

Ozçakar, Z.B., J. Foster II, O. Diaz-Horta, O. Kasapcopur, Y.S. Fan, F. Yalçınkaya, and M. Tekin. 2013. DNASE1L3 mutations in hypocomplementemic urticarial vasculitis syndrome. *Arthritis Rheum.* 65: 2183–2189. https://doi.org/10.1002/art.38010

Paharik, A.E., and A.R. Horswill. 2016. The staphylococcal biofilm: Adhesins, regulation, and host response. *Microbiol. Spectr.* 4:4. https://doi.org/10.1128/microbiolspec.VMBF-0022-2015

Rice, K.C., E.E. Mann, J.L. Endres, E.C. Weiss, J.E. Cassat, M.S. Smeltzer, and K.W. Bayles. 2007. The cidA murein hydrolase regulator contributes to DNA release and biofilm development in *Staphylococcus aureus*. *Proc. Natl. Acad. Sci. USA.* 104:8113–8118. https://doi.org/10.1073/pnas.0610226104

Robertson, C.M., E.E. Perrone, K.W. McConnell, W.M. Dunne, B. Boody, T. Brahmbhatt, M.J. Diacovo, N. Van Rooijen, L.A. Hogue, C.L. Cannon, et al. 2008. Neutrophil depletion causes a fatal defect in murine pulmonary *Staphylococcus aureus* clearance. *J. Surg. Res.* 150:278–285. https://doi.org/10.1016/j.jss.2008.02.009

Sánchez-Romero, M.A., I. Cota, and J. Casadesús. 2015. DNA methylation in bacteria: From the methyl group to the methylome. *Curr. Opin. Microbiol.* 25:9–16. https://doi.org/10.1016/j.mib.2015.03.004

Sauer, K., P. Stoodley, D.M. Goeres, L. Hall-Stoodley, M. Burmølle, P.S. Stewart, and T. Bjarnsholt. 2022. The biofilm life cycle: Expanding the conceptual model of biofilm formation. *Nat. Rev. Microbiol.* 20:608–620. https://doi.org/10.1038/s41579-022-00767-0

Seong, C.-S., A. Varela-Ramirez, and R.J. Aguilera. 2006. DNase II deficiency impairs innate immune function in *Drosophila*. *Cell. Immunol.* 240:5–13. https://doi.org/10.1016/j.cellimm.2006.05.007

Seredkina, N., and O.P. Rekvig. 2011. Acquired loss of renal nuclease activity is restricted to DNaseI and is an organ-selective feature in murine lupus nephritis. *Am. J. Pathol.* 179:1120–1128. https://doi.org/10.1016/j.ajpath.2011.05.011

Serpas, L., R.W.Y. Chan, P. Jiang, M. Ni, K. Sun, A. Rashidfarrokhi, C. Soni, V. Sisirak, W.S. Lee, S.H. Cheng, et al. 2019. Dnase1l3 deletion causes aberrations in length and end-motif frequencies in plasma DNA. *Proc. Natl. Acad. Sci. USA.* 116:641–649. https://doi.org/10.1073/pnas.1815031116

Sharma, K., and A. Pagedar Singh. 2018. Antibiofilm effect of DNase against single and mixed species biofilm. *Foods.* 7:42. https://doi.org/10.3390/foods7030042

Shi, X., R.W. Siggins, W.L. Stanford, J.N. Melvan, M.D. Basson, and P. Zhang. 2013. Toll-like receptor 4/stem cell antigen 1 signaling promotes hematopoietic precursor cell commitment to granulocyte development during the granulopoietic response to *Escherichia coli* bacteremia. *Infect. Immun.* 81:2197–2205. https://doi.org/10.1128/IAI.01280-12

Shiokawa, D., T. Matsushita, Y. Shika, M. Shimizu, M. Maeda, and S. Tanuma. 2007. DNase X is a glycosylphosphatidylinositol-anchored membrane enzyme that provides a barrier to endocytosis-mediated transfer of a foreign gene. *J. Biol. Chem.* 282:17132–17140. https://doi.org/10.1074/jbc.M610428200

Sisirak, V., B. Sally, V. D'Agati, W. Martinez-Ortiz, Z.B. Özçakar, J. David, A. Rashidfarrokhi, A. Yeste, C. Panea, A.S. Chida, et al. 2016. Digestion of chromatin in apoptotic cell microparticles prevents autoimmunity. *Cell.* 166:88–101. https://doi.org/10.1016/j.cell.2016.05.034

Soni, C., O.A. Perez, W.N. Voss, J.N. Pucella, L. Serpas, J. Mehl, K.L. Ching, J. Goike, G. Georgiou, G.C. Ippolito, et al. 2020. Plasmacytoid dendritic cells and type I interferon promote extrafollicular B cell responses to extracellular self-DNA. *Immunity.* 52:1022–1038.e7. https://doi.org/10.1016/j.immuni.2020.04.015

Tam, K., K.A. Lacey, J.C. Devlin, M. Coffre, A. Sommerfield, R. Chan, A. O'Malley, S.B. Koralov, P. Loke, and V.J. Torres. 2020. Targeting leukocidin-mediated immune evasion protects mice from *Staphylococcus aureus* bacteremia. *J. Exp. Med.* 217:217. https://doi.org/10.1084/jem.20190541

Tetz, G.V., N.K. Artemenko, and V.V. Tetz. 2009. Effect of DNase and antibiotics on biofilm characteristics. *Antimicrob. Agents Chemother.* 53: 1204–1209. https://doi.org/10.1128/AAC.00471-08

Thammavongsa, V., D.M. Missiakas, and O. Schneewind. 2013. Staphylococcus aureus degrades neutrophil extracellular traps to promote immune cell death. *Science.* 342:863–866. https://doi.org/10.1126/science.1242255

Thomer, L., O. Schneewind, and D. Missiakas. 2016. Pathogenesis of *Staphylococcus aureus* bloodstream infections. *Annu. Rev. Pathol.* 11:343–364. https://doi.org/10.1146/annurev-pathol-012615-044351

Thomsen, I.P., and G.Y. Liu. 2018. Targeting fundamental pathways to disrupt *Staphylococcus aureus* survival: Clinical implications of recent discoveries. *JCI Insight.* 3:e98216. https://doi.org/10.1172/jci.insight.98216

Thurlow, L.R., G.S. Joshi, and A.R. Richardson. 2012. Virulence strategies of the dominant USA300 lineage of community-associated methicillin-resistant *Staphylococcus aureus* (CA-MRSA). *FEMS Immunol. Med. Microbiol.* 65:5–22. https://doi.org/10.1111/j.1574-695X.2012.00937.x

Volkman, H.E., and D.B. Stetson. 2014. The enemy within: Endogenous retroelements and autoimmune disease. *Nat. Immunol.* 15:415–422. https://doi.org/10.1038/ni.2872

Wagener, J.S., and O. Kupfer. 2012. Dornase alfa (Pulmozyme). *Curr. Opin. Pulm. Med.* 18:609–614. https://doi.org/10.1097/MCP.0b013e328358d51f

Walker, T.S., K.L. Tomlin, G.S. Worthen, K.R. Poch, J.G. Lieber, M.T. Saavedra, M.B. Fessler, K.C. Malcolm, M.L. Vasil, and J.A. Nick. 2005. Enhanced *Pseudomonas aeruginosa* biofilm development mediated by human neutrophils. *Infect. Immun.* 73:3693–3701. https://doi.org/10.1128/IAI.73.6.3693-3701.2005

Weisenburger, T., B. von Neubeck, A. Schneider, N. Ebert, D. Schreyer, A. Acs, and T.H. Winkler. 2018. Epistatic interactions between mutations of deoxyribonuclease 1-like 3 and the inhibitory Fc gamma receptor IIB result in very early and massive autoantibodies against double-stranded DNA. *Front. Immunol.* 9:1551. https://doi.org/10.3389/fimmu.2018.01551

Wertheim, H.F., D.C. Melles, M.C. Vos, W. van Leeuwen, A. van Belkum, H.A. Verbrugh, and J.L. Nouwen. 2005. The role of nasal carriage in *Staphylococcus aureus* infections. *Lancet Infect. Dis.* 5:751–762. https://doi.org/10.1016/S1473-3099(05)70295-4

Wilber, A., M. Lu, and M.C. Schneider. 2002. Deoxyribonuclease I-like III is an inducible macrophage barrier to liposomal transfection. *Mol. Ther.* 6: 35–42. https://doi.org/10.1006/mthe.2002.0625

Xiong, Y.Q., J. Willard, J.L. Kadurugamuwa, J. Yu, K.P. Francis, and A.S. Bayer. 2005. Real-time in vivo bioluminescent imaging for evaluating the efficacy of antibiotics in a rat *Staphylococcus aureus* endocarditis model. *Antimicrob. Agents Chemother.* 49:380–387. https://doi.org/10.1128/AAC.49.1.380-387.2005

Yang, C., and M. Montgomery. 2021. Dornase alfa for cystic fibrosis. *Cochrane Database Syst. Rev.* 3:CD001127. https://doi.org/10.1002/14651858.CD001127

Yasutomo, K., T. Horiuchi, S. Kagami, H. Tsukamoto, C. Hashimura, M. Urushihara, and Y. Kuroda. 2001. Mutation of DNASE1 in people with systemic lupus erythematosus. *Nat. Genet.* 28:313–314. https://doi.org/10.1038/91070

Zapotoczna, M., E. O'Neill, and J.P. O'Gara. 2016. Untangling the diverse and redundant mechanisms of *Staphylococcus aureus* biofilm formation. *PLoS Pathog.* 12:e1005671. https://doi.org/10.1371/journal.ppat.1005671

Zervou, M.I., A. Andreou, M. Matalliotakis, D.A. Spandidos, G.N. Goulielmos, and E.E. Eliopoulos. 2020. Association of the DNASE1L3 rs35677470 polymorphism with systemic lupus erythematosus, rheumatoid arthritis and systemic sclerosis: Structural biological insights. *Mol. Med. Rep.* 22:4492–4498. https://doi.org/10.3892/mmr.2020.11547

Zykova, S.N., A.A. Tveita, and O.P. Rekvig. 2010. Renal Dnase1 enzyme activity and protein expression is selectively shut down in murine and human membranoproliferative lupus nephritis. *PLoS One.* 5:e12096. https://doi.org/10.1371/journal.pone.0012096

Supplemental material

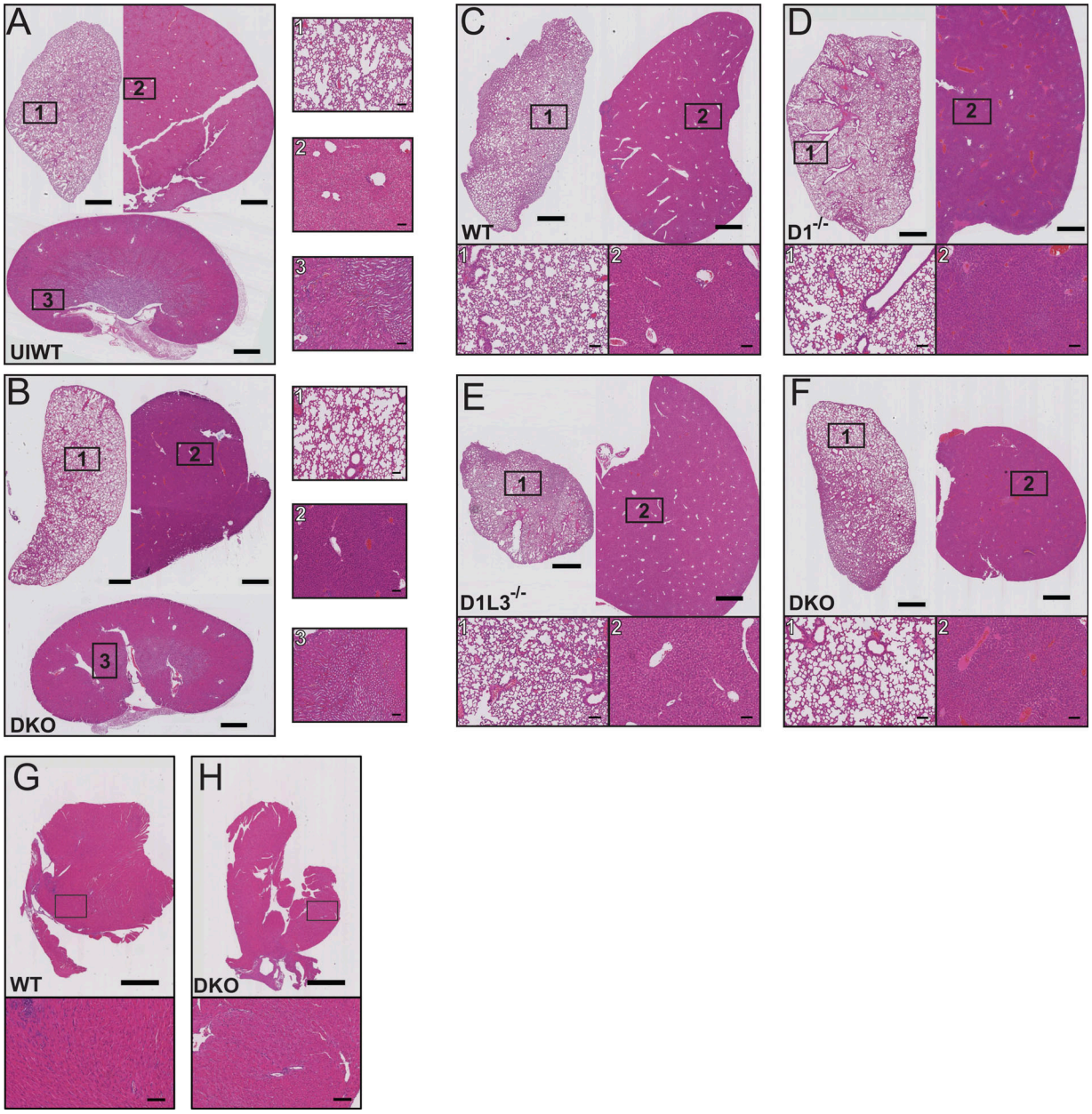

Figure S1. **Organ pathology after systemic infection with *S. aureus*. (A and B)** Representative H&E-stained sections of lungs (1), liver (2), and kidneys (3) from uninfected WT (UIWT) mice (A) and $D1^{-/-}D1L3^{-/-}$ (DKO) mice (B) 18 h after infection with *S. aureus*. **(C–H)** Representative H&E-stained sections of lungs (1) and liver (2) from WT (C), $D1^{-/-}$ (D), $D1L3^{-/-}$ (E), and $D1^{-/-}D1L3^{-/-}$ (DKO; F) and heart from WT (G) and $D1^{-/-}D1L3^{-/-}$ (H) mice 72 h after infection with *S. aureus*. Shown are low-magnification images of organs (scale bar, 1 mm) and high-magnification images of areas highlighted in black rectangles (scale bar, 100 µm).

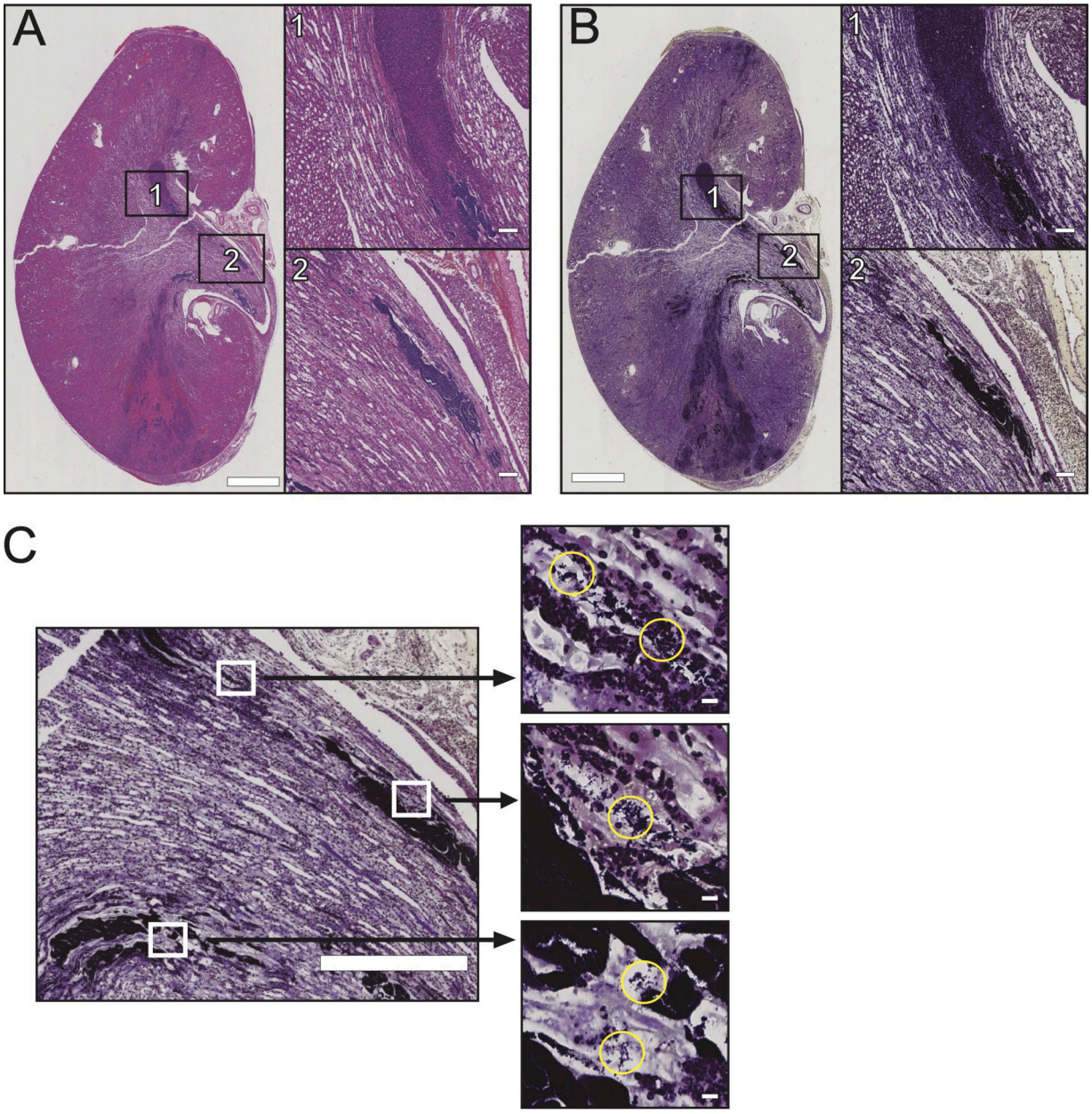

Figure S2. **Gram-positive staphylococci in the kidneys of infected mice. (A and B)** Representative serial sections of a kidney from a $D1^{-/-}D1L3^{-/-}$ mouse 72 h after infection with *S. aureus* were stained with H&E (A) or Gram stain (B). Each panel shows a low-magnification image (scale bar, 1 mm) and high-magnification images of areas highlighted in black rectangles (scale bar, 100 µm). **(C)** Further magnification of a Gram-stained section with select regions with Gram-positive staphylococci, indicated by yellow.

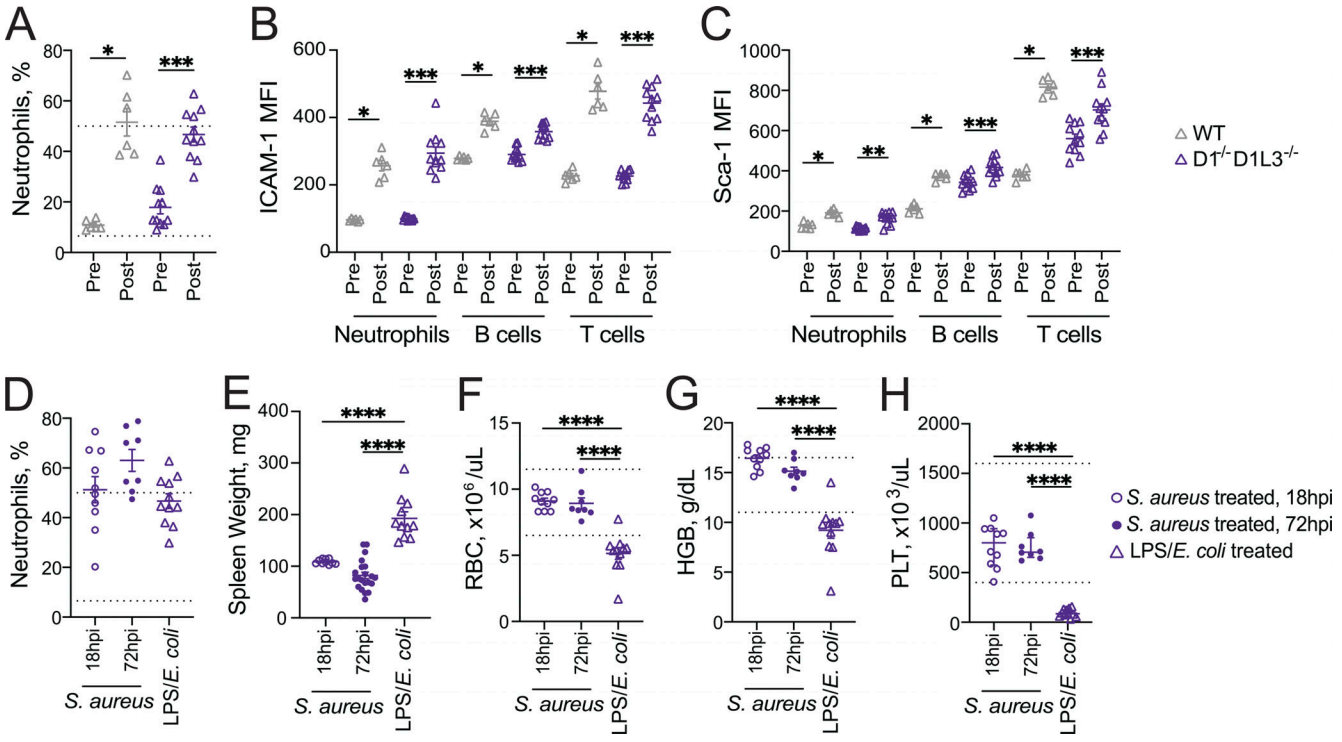

Figure S3. **Induction of neutrophilia by *S. aureus* infection and sterile inflammation. (A–C)** WT or D1$^{-/-}$D1L3$^{-/-}$ mice were given three doses of LPS and one dose of heat-killed *E. coli* and sacrificed 24 h later. Shown is the fraction of blood neutrophils measured by CBC (A) and the mean fluorescent intensity (MFI) of ICAM-1 (B) and Sca-1 (C) on the indicated cell types in the peripheral blood measured by flow cytometry at baseline (pre) and 24 h after *E. coli* injection. Symbols represent individual mice; bars represent mean ± SEM; dotted lines represent the range of normal values for CBC. **(D–H)** D1$^{-/-}$D1L3$^{-/-}$ mice were treated as above or infected with 1 × 10^7 CFU of *S. aureus* and sacrificed 18 or 72 h after infection (hpi). Shown is the fraction of neutrophils in the peripheral blood measured by CBC (D); spleen weight (E); and red blood cell count (F), hemoglobin concentration (G), and platelet count (H) in the peripheral blood measured by CBC. Symbols represent individual mice; bars represent mean ± SEM; dotted lines represent the range of normal values. Statistical significance was determined by Wilcoxon matched-pairs signed rank test (A–C) and two-way ANOVA followed by Tukey's multiple-comparison test (D–H). Two-tailed P values < 0.05 (*), <0.01 (**), <0.001 (***), and <0.0001 (****).

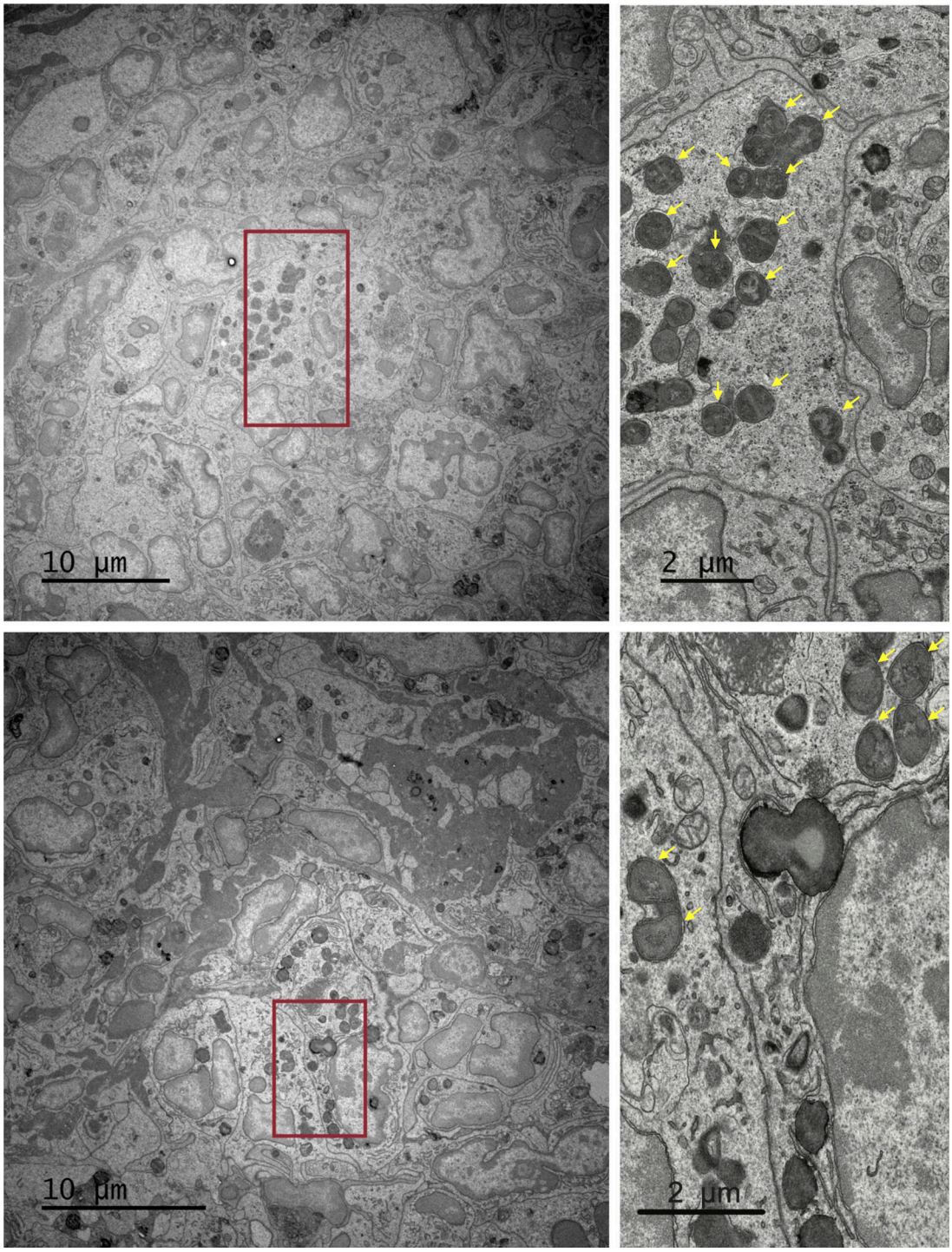

Figure S4. **Detection of *S. aureus* in the kidney by transmission EM.** Shown are representative transmission EM images of kidneys from D1$^{-/-}$D1L3$^{-/-}$ mice 72 h after infection with 1 × 10^7 CFU of *S. aureus* (scale bars, 10 µm). Areas highlighted in red rectangles are shown at higher magnification on the right (scale bars, 2 µm). The *S. aureus* cells, represented by dense round structures circumscribed by capsules and with an occasional internal septum, are highlighted by arrows.

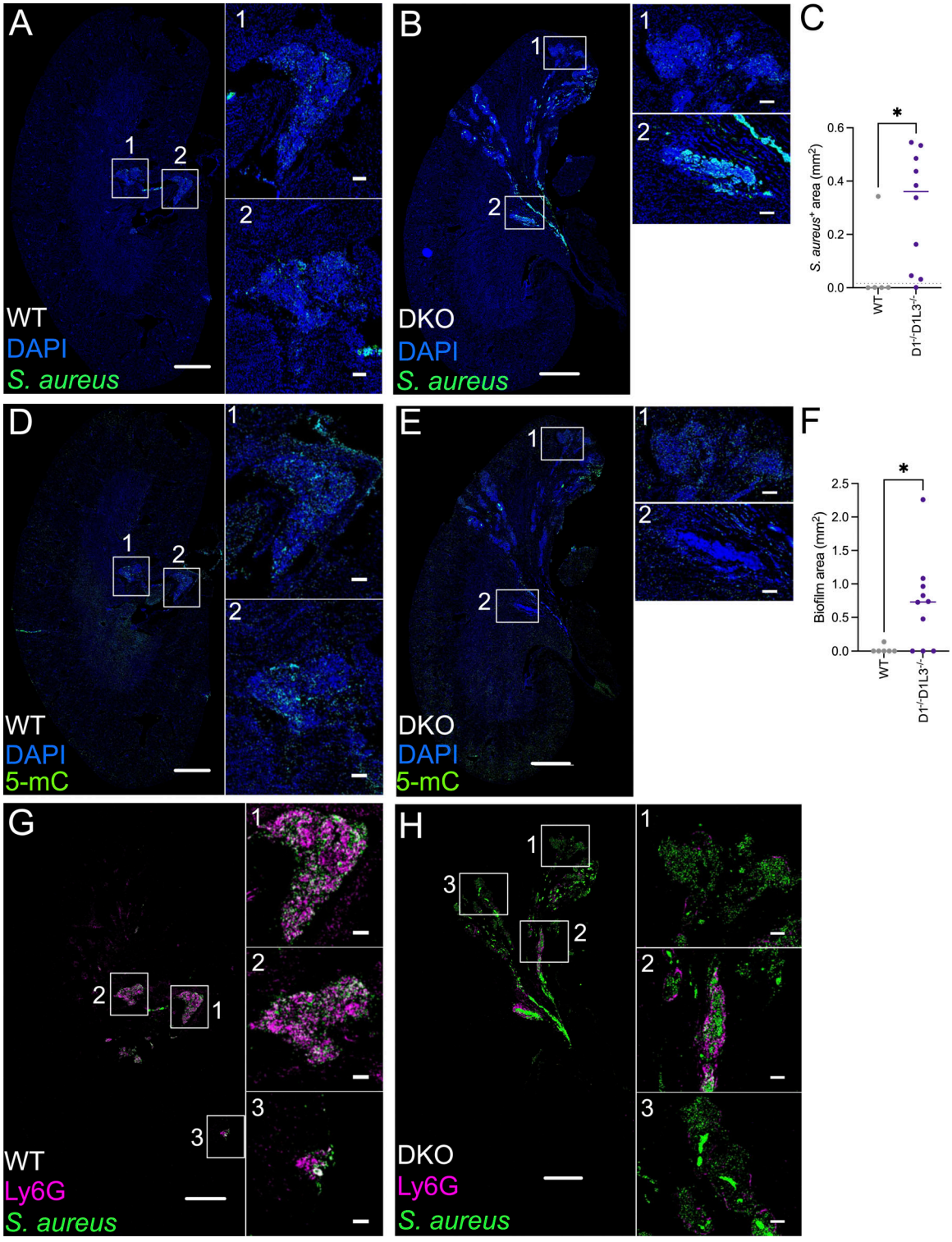

Figure S5. **Biofilm formation in the kidneys at 48 h after infection with *S. aureus*.** WT or D1$^{-/-}$D1L3$^{-/-}$ DKO mice were infected i.v. with 1 × 10^7 CFU of *S. aureus*, and their kidneys were examined by immunohistochemistry 48 h later. **(A and B)** Kidney sections from infected WT (A) and DKO (B) mice stained with anti–*S. aureus* antibody and DAPI. Shown are low-magnification images of the entire kidney (scale bar, 1 mm) and magnified images of areas in white boxes (scale bar, 100 µm). **(C)** Quantification of *S. aureus*–positive area in kidney sections. Symbols represent individual mice; bars represent median. The dotted line represents the mean value of uninfected WT mice. **(D and E)** Kidney sections of WT (D) and DKO (E) mice stained with DAPI and 5-mC. Each panel includes low-magnification images of the entire kidney (scale bar, 1 mm) and magnified images of areas in white boxes (scale bar, 100 µm). **(F)** Quantification of DAPI-positive 5-mC–negative biofilm area in kidney sections. Symbols represent individual mice; bars represent the median. Serial sections were taken from the same kidney for *S. aureus* and 5-mC staining. **(G and H)** Kidney sections from infected WT (G) and DKO (H) mice stained with antibodies to *S. aureus* and Ly-6G. Shown are low-magnification images of the entire kidney (scale bar, 1 mm) and magnified images of areas in white boxes (scale bars, 100 µm). Representative of three to four animals per group. Statistical significance was determined by Mann–Whitney test; two-tailed P values <0.05 (*).

Video 1. **Serial block-face scanning EM of a bacterial lesion in the kidney.** Kidneys from D1$^{-/-}$D1L3$^{-/-}$ mice 72 h after infection with 10^7 CFU of *S. aureus* were imaged by serial scanning EM. Shown is a Z-stack of 480 slices covering 48 µm of a 90 × 90 µm area; bacteria are pseudocolored in green. Playback speed, 30 frames per second.